Catena 138 (2016) 52–67

Contents lists available at ScienceDirect

Catena

journal homepage: www.elsevier.com/locate/catena

Cosmogenic age constraints on post-LGM catastrophic rock slope failures in the Tatra Mountains (Western Carpathians)

Tomáš Pánek [a], Zbyněk Engel [b], Pavel Mentlík [c,*], Régis Braucher [d], Michal Břežný [a], Václav Škarpich [a], Albert Zondervan [e]

[a] Department of Physical Geography and Geoecology, Faculty of Science, University of Ostrava, Chittussiho 10, 710 00 Ostrava, Czech Republic
[b] Department of Physical Geography and Geoecology, Charles University in Prague, Albertov 6, 12843 Praha, Czech Republic
[c] Centre of Biology, Geoscience and Environmental Education, University of West Bohemia, Plzeň, Czech Republic
[d] Aix-Marseille Université, CEREGE, CNRS UM 34, F-13545 Aix-en-Provence, France
[e] Environment and Materials Division, GNS Science, Lower Hutt, New Zealand

ARTICLE INFO

Article history:
Received 30 June 2015
Received in revised form 19 October 2015
Accepted 10 November 2015
Available online 6 December 2015

Keywords:
Rock slope failures
LGM
Paraglacial setting
^{10}Be dating
Western Carpathians
Tatra Mountains

ABSTRACT

Although deglaciation is one of the crucial factors controlling the stability of slopes in high mountains, the chronological response of rock slope failure (RSF) to glacier retreat still remains poorly known. Here we provide the first cosmogenic (^{10}Be) age constraints on prominent rock avalanches and rockfalls (collectively termed 'rock slope failures' – RSFs) from the Tatra Mountains, the highest mountain range with the most pronounced glacier morphology within the Carpathians. Six representative RSFs were selected for surface exposure dating in the mountain range. Two sites are situated in the western part with less pronounced local relief and gentler slope gradient, and four come from the highest eastern part with oversteepened rock slopes. Our dataset also contains the largest known RSF in the Tatra Mountains; the Koprová rock avalanche with a volume of ~5.4×10^6 m^3. Based on 26 ^{10}Be dated boulders, the weighted mean ages of individual RSF accumulations range between 20.2 ± 1.2 and 10.1 ± 0.3 ka. Our results suggest that smaller, structurally predisposed failures (mainly rockfalls) in the steepest parts of the mountains reacted immediately (i.e. a few hundred years) to deglaciation, whereas more complex slope deformations in terrain with lower local relief, involving the largest rock avalanche in the Tatra Mountains, experienced a substantial time lag (i.e. several millennia) in respect to ice retreat. In the case of delayed RSFs, their origin can be well correlated with warmer and more humid periods in the Lateglacial/early Holocene such as the Bølling–Allerød chronozone and after the onset of the Holocene.

1. Introduction

Catastrophic rock slope failures (RSFs) involving rock avalanches, rockslides and rockfalls are very efficient geomorphic agents and hazardous phenomena in mountain areas (Korup et al., 2010). They frequently occur in deglaciated landscapes, including regions which underwent glacier retreat during the Late Pleistocene (Cossart et al., 2008; Ballantyne et al., 2014a, 2014b) and in mountains experiencing recent glacier thinning following the Little Ice Age glacier culmination (Holm et al., 2004; Allen et al., 2011). However, although the abundance of RSFs within deglaciated areas is well known (Cossart et al., 2014), their chronological link to local deglaciation patterns is still poorly understood and in fact limited to only a few world regions containing larger datasets of dated RSFs and well reconstructed deglaciation histories, such as Scotland (Ballantyne et al., 2013, 2014a, 2014b), Norway (Blikra et al., 2006; Longva et al., 2009) and the European Alps (Cossart et al., 2008; Prager et al., 2008). Theoretical models dealing with RSF response to ice retreat usually consider the highest frequency of slope instabilities immediately after deglaciation, with a gradual or abrupt decline of RSF frequency thereafter (Cruden and Hu, 1993). However, growing datasets of numerically dated RSFs reveal that a chronological relationship between the deglaciation and origin of slope failures is more complicated (Prager et al., 2008; Ballantyne et al., 2014a, 2014b), reflecting the complexity of rock mass properties and diverse slope-destabilizing processes (e.g. slope debutressing, permafrost degradation, seismicity related to isostatic rebound, meltwater effects) accompanying the withdrawal of glaciers from mountain valleys (McColl, 2012). In such circumstances, RSFs are very often significantly delayed in respect to deglaciation, involving time lags in orders of 10^2–10^4 yrs. (Ballantyne et al., 2014a, 2014b). Therefore, determination of the age of RSFs in various types of paraglacial landscapes (Ballantyne, 2002) with better understanding of the rock slopes' responses to glacier withdrawal remains an important interdisciplinary task for understanding mountain landscape development. Recent progress in terrestrial cosmogenic nuclide (TCN) dating provides a great opportunity for RSF age determinations. Although the number of studies using TCN for timing slope failures is still rather low in

* Corresponding author.
E-mail address: pment@cbg.zcu.cz (P. Mentlík).

http://dx.doi.org/10.1016/j.catena.2015.11.005
0341-8162/

comparison with applications in glacial and fluvial geomorphology (Pánek, 2015), successful age determination of several RSFs throughout the world indicate the great potential of this method in the field of dating mass movements (e.g. Hormes et al., 2008; Ivy-Ochs et al., 2009; Dortch et al., 2009; Hewitt et al., 2011; Penna et al., 2011; Yuan et al., 2013; Ballantyne et al., 2014a, 2014b; Claude et al., 2014; Hughes et al., 2014; Zerathe et al., 2014; Nagelisen et al., 2015).

In this paper, we provide the first cosmogenic ^{10}Be dating of large RSFs from the Tatra Mountains (Slovakia), the highest mountain range in the Carpathians (Fig. 1). The aims of this study are: (i) to describe typical modes, kinematics and geomorphology of RSFs within the granodiorites of the Tatra Mountains, (ii) to provide cosmogenic ^{10}Be dating of the most representative prehistoric RSFs situated in this area and (iii) to correlate the timing of RSFs with local Late Pleistocene deglaciation history. Due to the limited area, homogenous geology and well-constrained deglaciation chronology (Makos et al., 2012, 2013, 2014; Engel et al., 2015), this region represents an excellent natural laboratory for the study of the chronological links between glacier retreat and RSF origin.

2. Regional settings

2.1. Geology, tectonics and origin of recent topography

The Tatra Mountains (49°05′–49°20′ N, 19°33–20°25′ E) are situated along the Slovakian/Polish border, in the culmination part of the Western Carpathians (Fig. 1). With the highest point of the Gerlachovský peak (2654 m a.s.l.), it is the highest mountain range in the whole Carpathian mountain system. Although the mountain area is limited in size (the longest W-E axis of the range is about 55 km), it represents a distinct geomorphic unit with rugged rocky relief rising 1000–1500 m above the surrounding basins. The western part of the mountains (called Western Tatra Mountains) is somewhat lower (the summit level is about 2000 m of elevation) and characterized by gentler hillslopes, whereas the eastern section (called Eastern "High" Tatra Mountains) contains a high concentration of peaks exceeding 2400 m of elevation (Fig. 2).

The geological structure is dominated by the Tatric crystalline basement represented by Variscan/Carboniferous biotitic granodiorite and to a lesser extent also ortho-and paragneisess (Němčok et al., 1994). Crystalline rocks are overlain by allochthonous Mesozoic nappes (Triassic and Jurassic limestones, quartzites, etc.), and contemporary outcropping as denudational remnants mainly on the northern slopes of the range (Němčok et al., 1994; Fig. 1). The Alpine tectonic structure of the mountains originated during several stages of tectonic deformations between the middle-Cretaceous and Quaternary periods (Králiková et al., 2014). Multistage tectonic deformations caused a substantial weakening of the bedrock, which is especially well-reflected within the granodiorite by the presence of numerous mylonite zones with reduced rock mass strength. The recent distinct topography mainly arises from the youngest phase of the uplift, which has occurred since the Miocene. Apatite fission track data from the highest granodiorite part of the mountains yield ages between ~37–9.3 Ma, with the majority of ages spanning between ~15 and 10 Ma (Králiková et al., 2014). The uplift of the mountain range was highly asymmetric and predominantly concentrated along the sub-Tatra fault forming the southern boundary of the area. It led to the overall northward tilting of the range, deep exhumation of the southern flank and evolution of a prominent fault scarp forming the southern boundary of the mountains (Fig. 1). The current seismicity of the Tatra Mountains is rather marginal with historical earthquakes reaching maximum moment magnitudes (M_w) of ~4.5–5.5 (Pagaczewski, 1972).

2.2. Last glaciation of the Tatra Mountains

Alongside the Late Neogene/Quaternary uplift, repeated glaciations during the Pleistocene were among the most important factors affecting the current topography of the Tatra Mountains (Lukniš, 1973). Situated midway between the Scandinavian and Alpine ice sheets, the Tatra Mountains was the most glaciated mountain area in central Europe during the global Last Glacial Maximum (LGM) (between 26.5 and 20–19 ka, Clark et al., 2009). The region hosted 55 glacier systems, which occupied a total of 280 km^2 and some individual glaciers reached lengths >13 km (Fig. 1). The largest glaciers attained thicknesses of up to 400 m (Zasadni and Kłapyta, 2014). ^{36}Cl and ^{10}Be ages of moraines

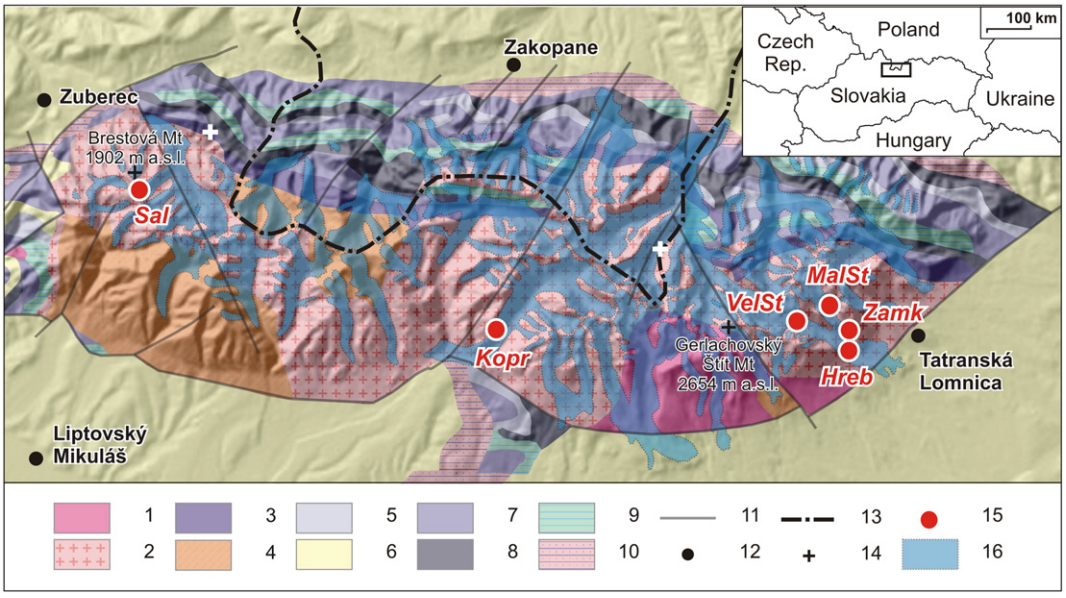

Fig. 1. Schematic geological map of the Tatra Mountains after Němčok et al. (1994) with marked dated RSFs and extent of glaciation during the LGM Legend: 1 — tonalite to granodiorite rocks (Carboniferous–Permian), 2 — granite rocks (Carboniferous–Permian), 3 — quartzite, sandstone and shale rocks (Triassic), 4 — amphibolite, migmatite and gneiss rocks (Paleozoic), 5 — shale, sandstone, limestone, dolomite and hornblende rocks (Middle–Upper Triassic), 6 — conglomerate, sandstone, marlstone, shale, calcareous-claystone and claystone flysch rocks (Cretaceous–Paleogene), 7 — limestone, dolomite and hornblende rocks (Triassic), 8 — limestone, sandstone, sandstone–limestone rocks (Triassic–Late Jurassic), 9 — layers of carbonate claystone, hornblende and marlstone rocks (Jurassic–Lower Cretaceous), 10 — conglomerate, sandstone, limestone, breccia and claystone rocks (Paleogene), 11 — faults, 12 — towns and municipalities, 13 — state border, 14 — mountain peaks, 15 — studied areas, 16 — LGM glaciers according to Zasadni and Kłapyta (2014).

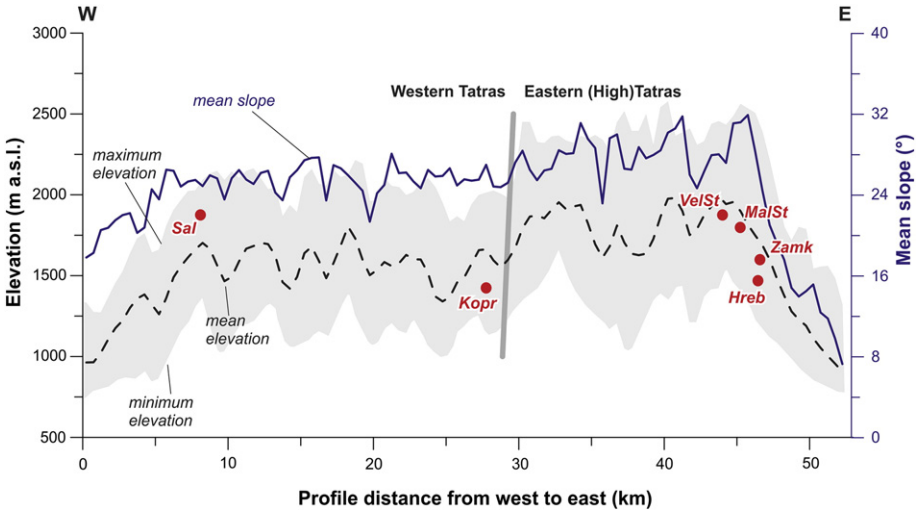

Fig. 2. Position of studied RSFs within west-east oriented swath profile of the Tatra Mountains showing mean slope gradient (°) and maximum, minimum and mean elevation.

and glacially polished surfaces throughout the mountains revealed that the local LGM took place between ~26 and 21.0–20.5 ka (Makos et al., 2014; Engel et al., 2015) with a suggested local maximum extent of Velká and Malá Valleys palaeoglacier ~22.0 ka (Engel et al., 2015). The last cirque glaciers disappeared after ~11 ka (Makos et al., 2012, 2013; Engel et al., 2015). The strong imprint of repeated Pleistocene glaciations is reflected in the abundance of glacial landforms such as latero-terminal moraine loops, U-shape troughs, cirques, glacier trimlines and oversteepened rock slopes. The eastern part of the Tatra Mountains is dominated by rock relief with arêtes, pyramidal peaks and horns forming the highest peaks of the area. Besides glacial phenomena, common features are relict rock glaciers infilling valleys especially in the western part of the mountains (Němčok and Mahr, 1974; Kłapyta, 2013).

2.3. RSFs in the Tatra Mountains

Distribution of RSFs throughout the area is well known from the studies of Lukniš (1973); Mahr and Němčok (1977), and Němčok (1982). Slope deformations, involving mainly deep-seated "sackung"-type deformations of mountain ridges, rockfalls, landslides, debris flows and rock avalanches are frequent phenomena in the Tatra Mountains. However, in comparison with some other European high-mountain areas (e.g. the Alps, Pyrenees, Apennines, Scandinavian Mountains), RSFs in the Tatra Mountains reach only modest sizes with the majority of accumulations in orders of 10^3–10^5 m^3. Mass movements affect predominantly oversteepened rock slopes and thick unconsolidated glacial deposits. As demonstrated by Kalvoda (1994), zones of mylonitized and tectonically weakened granodiorites are especially prone to RSF. This is well reflected along the tectonic zone of the sub-Tatra fault, where numerous major RSF accumulations originated at the intersections of the southern boundary fault slope with N-S trending glacial valleys (Lukniš, 1973). Special attention was paid to the description of major accumulations of RSFs, such as the largest rock avalanche accumulation in the Koprová valley (~8×10^6 m^3 according to Lukniš, 1973) or rockfalls at the lower terminations of the Velká and Malá Studená valleys (Lukniš, 1973; Němčok, 1982). Although none of the RSFs have been hitherto dated in the Tatra Mountains, it was expected by some authors that the majority of failures took place just after the deglaciation at the beginning of the Holocene (Kotarba and Długosz, 2010).

3. Methods

3.1. Selection of study sites

Six representative RSFs from the Slovakian part of the Tatra Mountains were selected for ^{10}Be dating and geomorphic/kinematic analysis. All of the sites are situated within the lithologically homogenous granodiorite bedrock. In order to include RSFs from diversified types of topography, we dated localities both from the Western and Eastern (High) Tatra Mountains (Fig. 2). Two sites (Salatín and Koprová) are situated in the western part of the mountains with less pronounced local relief and gentler slope gradient, and four of them (Malá Studená, Velká Studená, Zamkovského and Hrebienok) at the eastern part of the mountains with oversteepened rock slopes (Fig. 2). Four RSFs from the High Tatra Mountains are situated in the Velká and Malá Studená dolina Valleys (glacial troughs), for which detailed, post-LGM deglaciation history has recently been established by (Engel et al., 2015). These sites thus provide a scope for comparison of the local deglaciation chronology and associated rock slope collapses within particular sections of the glacial troughs. As distinguishing between RSFs and glacial moraines can be somewhat ambiguous, we selected for dating only the most typical landforms (e.g. with pronounced head scarps) and followed criteria for RSFs identification proposed by Hewitt (1999).

3.2. Geomorphic mapping and kinematic analysis of slope failures

The main information about the geomorphological context of selected RSFs situated in the High Tatra Mountains was derived from the existing "Geomorphological map of the High Tatra Mountains" published in the scale of 1:50,000 by Lukniš (1968). In order to recognize principal landform assemblages in detail, we performed geomorphic mapping for the surrounding area of each studied RSF. The main aim was to find the most suitable sites for ^{10}Be exposure dating and obtain information regarding types of slope failures and their relationships with adjacent landforms, with a special focus on glacial landforms and deposits. Field GPS mapping was supported by the interpretation of aerial photographs and a photogrametrically derived digital elevation model (5-m grid DEM), which was launched by the EUROSENSE-group in 1998–2009 and finally updated in 2012. Mass movement products were classified according to the landslide classification of Cruden and Varnes (1996) and Hungr et al. (2014). Volumes and other metrics of RSFs were derived from the 5-m DEM, locally corrected by field measurements.

For better understanding of relationships between the bedrock structure and RSFs, extensive structural measurements of discontinuities (dip and dip directions; in total >1500 measurements) and kinematic analysis were performed throughout the head scarp areas of four RSFs (Salatín, Koprová, Zamkovského and Hrebienok). Kinematic analysis (e.g. Wyllie and Mah, 2004; Brideau et al., 2006, 2011; Stead et al., 2006) using Dips 6.0 software (Rocscience, 2014) was performed to determine possible failure modes (i.e. sliding, toppling or wedge failure). Because of the lack of information about real friction angles, two different values of φ were used. The upper value $\varphi = 34°$ represents the lower range of the typical values for coarse grained granitic/granodiorite rocks (Wyllie and Mah, 2004). The lower value ($\varphi = 20°$) was chosen in order to have a less strict criterion which could reflect e.g. weathered and/or tectonically weakened rocks. Lateral limits for planar, direct and flexural toppling failure mode were set to 20°. Although kinematic analysis for the two remaining RSFs (Velká Studená and Malá Studená) was not possible due to the extreme terrain conditions and inaccessibility of rock outcrops for structural measurements, their possible kinematic modes were inferred by the detailed inspection of depletion zones using high resolution aerial photographs.

3.3. TCN dating

We used cosmogenic ^{10}Be exposure dating of boulders within accumulation areas as the main tool for determining the age of selected RSFs. This dating strategy has been hitherto most frequently applied in the case of RSF dating (e.g. Hermanns et al., 2001; Dortch et al., 2009; Hewitt et al., 2011; Penna et al., 2011; Yuan et al., 2013; Ballantyne et al., 2014a, 2014b; Hughes et al., 2014; Nagelisen et al., 2015), although studies concerning exposure dating of head scarps have also been published recently (Recorbet et al., 2010; Zerathe et al., 2013, 2014; Lebourg et al., 2014). The reason why we are concerned solely with the boulder accumulations is that the head scarps of the studied RSFs are represented either by extremely steep rock faces with markers of subsequent collapses and thus with a high risk of exposure age rejuvenations (Velká Studená, Malá Studená, Zamkovského and Hrebienok) or by soil-covered slopes without relevant bedrock outcrops (Salatín and Koprová).

Altogether 26 granodiorite boulders from six RSF accumulations were sampled. The number of sampled boulders per RSF was determined with respect to the size and complexity of individual accumulations. Two to three samples were taken from the small and morphologically pronounced accumulations of the Velká Studená (n = 2) and the Salatín (n = 3) RSFs and at least five boulders were sampled at the large and more complex accumulations of Koprová, Malá Studená, Zamkovského and Hrebienok RSFs (Fig. 3). Sampled boulders were carefully selected in order to avoid any pre-failure radionuclide inheritance (i.e. boulders originally situated close to the original surface) or post-deposition changes (e.g. by erosion, toppling, exhumation from sediment cover). To do so, we sampled only upright boulders protruding >1 m above the surrounding surface. In order to minimize the possibility of sampling younger rockfalls, we sampled boulders situated in the terminal part of accumulations far from steep rock slopes. All samples for exposure dating were collected by chiselling the upper surfaces of quartz-rich granodiorite boulders. The thickness of the samples, topographic shielding and overall geometry (dip, height etc.) of the sampled surfaces were recorded.

The collected samples were distributed to two AMS facilities. The Salatín samples SalA1–3 were analysed by the XCAMS facility at GNS Science, New Zealand (Zondervan et al., in press). All the others were analysed by ASTER, the French Accelerator Mass Spectrometry National Facility located in Aix en Provence. The methodologies for processing and measuring the samples at these laboratories are very similar. We proceed by describing the methods followed by the French facility and only significant deviations by the XCAMS facility are mentioned. After collection, the samples are crushed, sieved and cleaned with a mixture of HCl and H_2SiF_6. The extraction method for ^{10}Be ($T_{1/2} = 1.387 \pm 0.012$ Ma; Korschinek et al., 2010; Chmeleff et al., 2010) involves isolation and purification of quartz and elimination of meteoric ^{10}Be. After physical pretreatment, the XCAMS facility applied the following sequence of chemistry to extract pure quartz: 'hotdog rolling' of the sample material in 10% HCl, in a 5% HF + 3.5% HNO3 mixture, in pyrophosphoric acid, and in a hot H_2SO_4 + HNO_3 mixture. A weighed amount (~0.1 g) of a 3025 ppm solution of ^{9}Be was added to the decontaminated quartz. Beryllium was subsequently separated from the solution by successive anionic and cationic resin extraction and precipitation. The final precipitates were dried and heated to 800 °C to obtain BeO, and finally mixed with niobium powder prior to the measurements. The beryllium data were calibrated directly against the National Institute of Standards and Technology beryllium standard reference material NIST SRM4325 by using an assigned value of $(2.79 \pm 0.03) \cdot 10^{-11}$. The XCAMS facility used ^{10}Be standard 01–5-1 with an assigned value of $2.709 \cdot 10^{-11}$ (Nishiizumi et al., 2007). Age uncertainties include AMS internal variability (<0.5%), an external AMS uncertainty of 0.5% (Arnold et al., 2010), blank correction and 1σ uncertainties. Long-term measurements of chemically processed blanks yield the ratios in the order of $(3.0 \pm 1.5) \cdot 10^{-15}$ for ^{10}Be. The XCAMS analysis involved correcting for the processing blank using a single analysis: $(1.7 \pm 0.6) \cdot 10^{5}$ at ^{10}Be. A sea-level, high-latitude spallation production of 4.03 ± 0.18 at·g^{-1} yr.$^{-1}$ was used and scaled for latitude (Stone, 2000) and elevation. This production rate is a weighted mean of the calibrated production rates in the Northern Hemisphere (Balco et al., 2009; Fenton et al., 2011; Goehring et al., 2012; Briner et al., 2012). All the individual production rates have been corrected relative to a ^{10}Be half-life of 1.387 Ma. The surface production rates were also corrected for the local slope and topographic shielding due to the surrounding terrain following Dunne et al. (1999). Cosmic rays exposure ages were calculated using the equation:

$$C_{(x,\varepsilon,t)} = \frac{P_{spall.}}{\frac{\varepsilon}{\Lambda_n}+\lambda} . e^{\frac{x}{\Lambda_n}} \left[1 - \exp\left\{-t\left(\frac{\varepsilon}{\Lambda_n}+\lambda\right)\right\}\right] + \frac{P_u}{\frac{\varepsilon}{\Lambda_\mu}+\lambda} . e^{\frac{x}{\Lambda_u}} \left[1 - \exp\left\{-t\left(\frac{\varepsilon}{\Lambda_\mu}+\lambda\right)\right\}\right]$$

where $C(x, \mathcal{E}, t)$ is the nuclide concentration as a function of depth x (g.cm^{-2}), $\mathcal{E}$ the denudation rate (g.cm^{-2}.a^{-1}), λ the radioactive decay constant (a^{-1}), and t the exposure time (a). P_{spall} and P_μ are the relative production rates due to neutrons and muons, respectively. Λ_n, Λ_μ are the effective apparent attenuation lengths (g.cm^{-2}), for neutrons and muons, respectively. The muon scheme follows Braucher et al. (2011). Multiple exposure ages obtained for a given accumulation were examined using a chi-square (χ^2) test and outliers were excluded from the dataset. Final datasets were used to calculate the error-weighted mean exposure age for a given accumulation. Exclusion of the negative and positive outliers (anomalies) to constrain ages of RSF accumulations is described and discussed in Ballantyne et al. (2013). Retrospective evaluation of negative anomalies identified at the Salatín and Hrebinok sites suggests block emplacement and toppling, respectively, after the main RSF events. Unless otherwise noted, all ages are reported as results of ^{10}Be dating.

4. Results

4.1. Geomorphology and relative age constraints of RSFs

The main characteristics of dated RSFs are presented in Table 1. Their landform assemblages are shown in geomorphic sketches (Fig. 3) and selected field photographs (Fig. 4). We focus especially on their

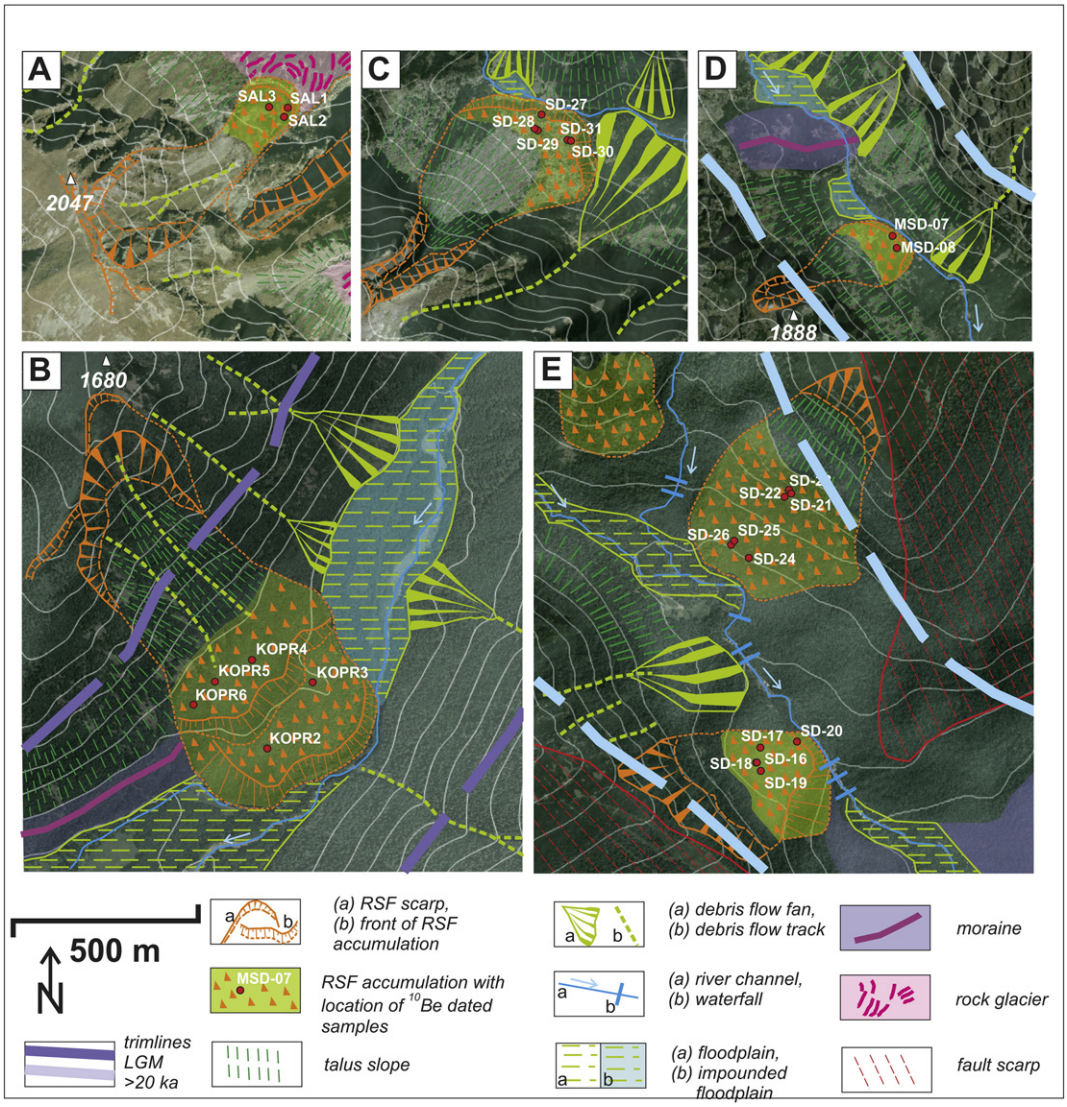

Fig. 3. Geomorphic maps denoting spatial context of studied RSFs and position of ^{10}Be-dated boulders. Aerial photographs with 50-m contours used as a background draped over 5-m grid shaded relief (A — Salatín; B — Koprová; C — Velká Studená; D — Malá Studená; E — Zamkovského and Hrebienok).

(i) overall geomorphic position, (ii) morphological and depositional peculiarities and (iii) relative timing.

All but one of the RSFs are situated on steep slopes of glacial troughs, one case (the Salatín RSF) occupies a cirque headwall (Fig. 3). Three RSFs (Koprová, Hrebienok, Zamkovského) are situated in the lowermost parts of troughs, at the mouths of valleys to the mountain piedmont (Figs. 3B, E). Two RSFs (Salatín and Koprová) are nested on slopes affected by deep-seated gravitational slope deformations (sackungen), suggesting prolonged evolution and possible recurrent behaviour of failures (Figs. 3A and B). All studied RSFs disrupt the LGM glacier trimline and some of them presumably also overlie coeval moraines (Koprová, Hrebienok; Fig. 5), which suggest their post-LGM age. In the case of the Salatín rock avalanche, its accumulation lobe is deposited on the rock glacier surface, causing its folding and the origin of crescentic mounds close to the front of the rock avalanche (Figs. 3A and 4A, B).

Considering the morphology of both depletion and accumulation zones together with runout parameters, volume and character of RSF material (Table 1; Figs 3 and 4), the studied failures can be classified as rock avalanches (i.e. lobate morphology, long runout, highly fragmented material; Koprová and Salatín RSFs) or rockfalls (i.e. accumulation consisting of chaotic boulders, limited runout, predominance of block-sized fractions; Velká Studená, Malá Studená and Hrebienok RSFs). The Zamkovského RSF, where the majority of accumulation is arrested on the slope, is consistent with characteristics typical for rockslides (Table 1; Figs. 3E, 4G and H). Only the Koprová RSF can be considered to be a typical rock avalanche, exceeding the nominal threshold volume of 1×10^6 m^3 proposed e.g. by Hsü (1975) or Hungr et al. (2001). The total volume of the largest RSF in the Tatra Mts. (calculated by using the 5-m-DEM) is ~5.4×10^6 m^3 (Table 1).

The internal morphology of the RSFs indicates that except for the Koprová and Hrebienok RSFs, the studied failures originated as single events. In the case of the Koprová rock avalanche, two overlapping lobes (volumes for the lower/older and overlying younger are ~3.8×10^6 m^3 and ~1.6×10^6 m^3, respectively) suggest that it originated as a polyphase failure with two generations of rock avalanches (Table 1; Figs. 3B and 5). As for the Hrebienok rockfall, the complex morphology of the accumulation zone with several longitudinal lobes together with a head scarp consisting of several chutes also indicate that this accumulation might have originated during multiple rockfall events (Figs. 3E and 4F). Another RSF, which was likely preceded by multiple failures, is the Salatín RSF. Although the accumulation of the Salatín rock avalanche originated as a single event, the volume of its head scarp (~2×10^6 m^3) contradicts the estimated volume of the rock avalanche deposit, which is about 0.3×10^6 m^3 (Table 1, Figs. 3A and 4A). Such a

Table 1
Main characteristics of dated RSFs.

Rock slope failure/used acronym	RSF area (km^2)	RSF aspect	Volume (10^3 m^3	Vertical range (m)	Length (m)	Fahrböschung (after Hsü (1975)) (°)	RSF classification**	Characteristics	
								Source area	Debris zone
Salatín/Sal	0.14	NE	300	397	750	27.9	Rock avalanche	Amphitheatre-shaped headscarp with missing volume (~10^6 m^3) significantly exceeding volume of debris accumulation; pronounced sackung scarps above the source area; strongly disrupted and tectonically weakened granodiorite bedrock (joint spacing ~5–10 cm).	Lobate accumulation with steep front deforms adjacent rock glacier forming compressional structures; only a few boulders protrude above the grassy surface.
Koprová (whole failure)/Kopr	0.46	ESE	5400	545	1100	26.4	Rock avalanche	Amphitheatre-shaped headscarp partly covered by talus; sackung scarps above the source area; partly predisposed by slope-parallel joint sets (dip ~50°); unstable rock face in the middle part of the headscarp is a potential source for recent rockfalls.	Large bouldery accumulation organized into two vertical steps revealing the older and younger generations of RSF.
Koprová 1st generation/Kopr1	0.22**	ESE	3800	545	1100	26.4	Rock avalanche	It cannot be distinguished between source areas of 1st and 2nd generations of RSFs.	At least 40 m thick bouldery accumulation with pronounced steep front; formerly dammed valley floor.
Koprová 2nd generation/Kopr2	0.09 **	ESE	1600	500	900	29.1	Rock avalanche	It cannot be distinguished between source areas of 1st and 2nd generations of RSFs.	Rises with the steep front above the surface of the 1st generation of RSF; partly covered by talus.
Velká Studená/VelSt	0.17	NE	700	535	800	33.8	Rockfall	Formed by the narrow wedge-like rock chute originated at the intersection of two joint sets; source area for numerous minor rockfalls.	Lobate accumulation with steep front formed mainly by large boulders (some of them >15 m in longer axis); substantial part of the accumulation covered by the younger talus cone.
Malá Studená/MalSt	0.05	NE	200	260	700	20.4	Rockfall	Formed by slope-parallel discontinuity plane.	Lobate accumulation with steep front formed mainly by large boulders, partly covered by talus.
Zamkovského/Zamk	0.23	SW	900	400	900	29.7	Rockfall	Facetted rock face predisposed by slope-parallel joint plane (dip ~45°); close vicinity to major sub-Tatra fault.	Accumulation formed mainly by large boulders (some of them >15 m in longer axis); without pronounced longitudinal lobes and steepened frontal part.
Hrebienok/Hreb	0.13	NE	300	300	500	31.0	Rockslide	Nearly vertical rock face disrupted by toppled rock pilars and chutes formed by the intersection of joint sets; close vicinity to major sub-Tatra fault, active toppling and minor rockfalls.	Accumulation formed mainly by large boulders (up to 5–10 m in the longer axis); pronounced longitudinal lobes and steepened frontal part.

*Only accumulation zone.
**In accordance with classifications of Cruden and Varnes (1996) and Hungr et al. (2014).

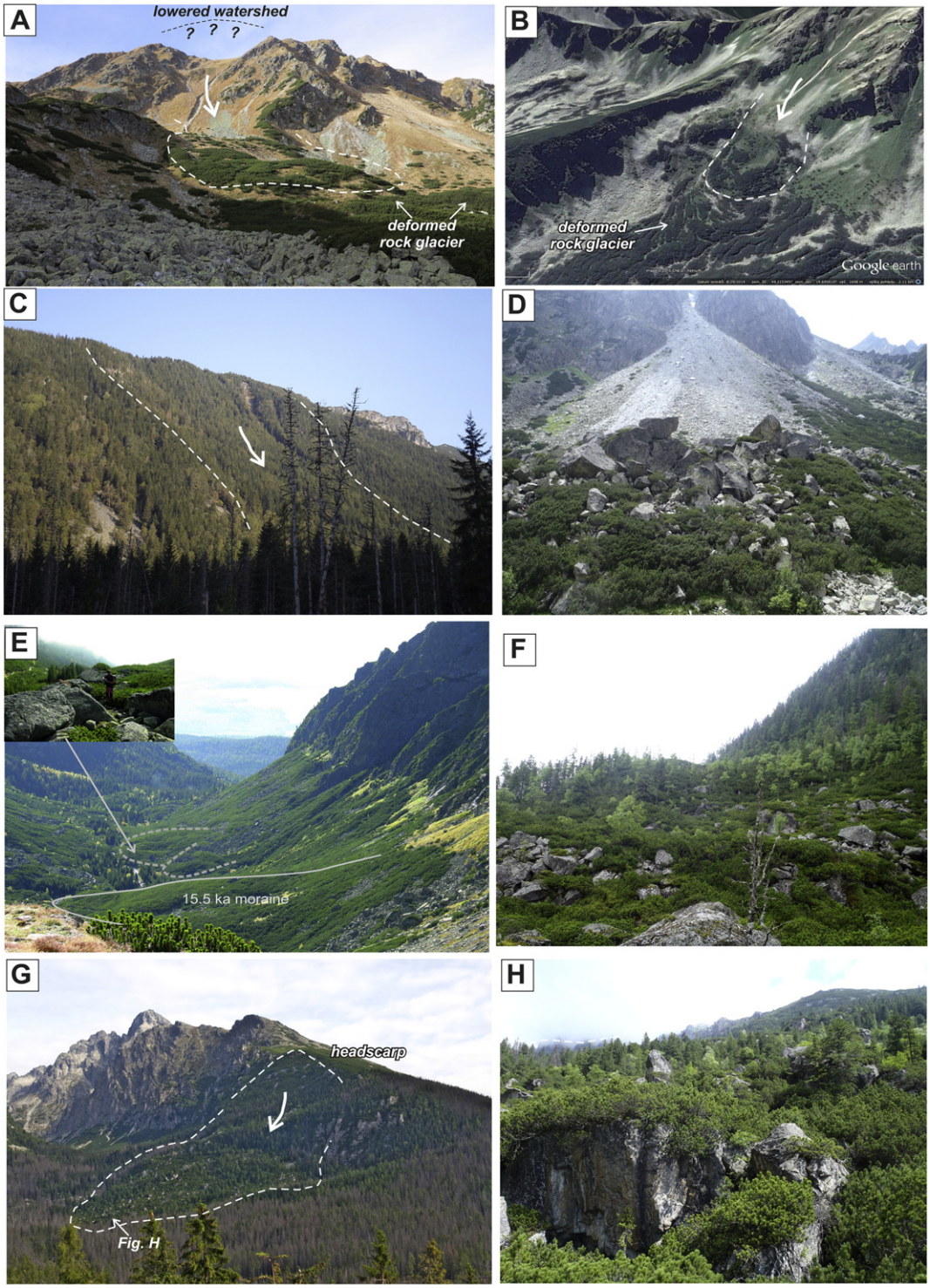

Fig. 4. Photographs of studied RSFs. A — Overall view of the Salatín rock avalanche. B — Google Earth image of the accumulation of the Salatín rock avalanche with deformed rock glacier at the forefield. C — Head scarp of the polyphase Koprová rock avalanche. D — Boulder accumulation of the Velká Studená rockfall partly overlain by talus deposits. E — Malá Studená rockfall situated in close vicinity of the ~15.5 ka moraine (Engel et al., 2015). F — Accumulation of the Hrebienok rockfall with several longitudinal lobes. G — Overall view of the Zamkovského rockslide with structurally-predisposed head scarp. H — Detailed view of large boulders within the accumulation of the Zamkovského rockslide.

discrepancy can be explained by multiple Late Pleistocene rock avalanches/rockfalls from the same source area, whereas only the youngest one persists in the recent landscape. The older generations of failures were probably removed by glacial erosion and/or consumed by the exceptionally large rock glacier that fills the cirque bottom of the Salatínská dolina Valley (Figs. 3A and 4B).

4.2. Kinematics of RSFs

Geomorphic observations of landforms and structures (e.g. sackung-type features) in their depletion zones suggest that the mechanism of both RSFs from the western part of the Tatra Mountains (Salatín and Koprová rock avalanches) was rather complex. Kinematic analysis

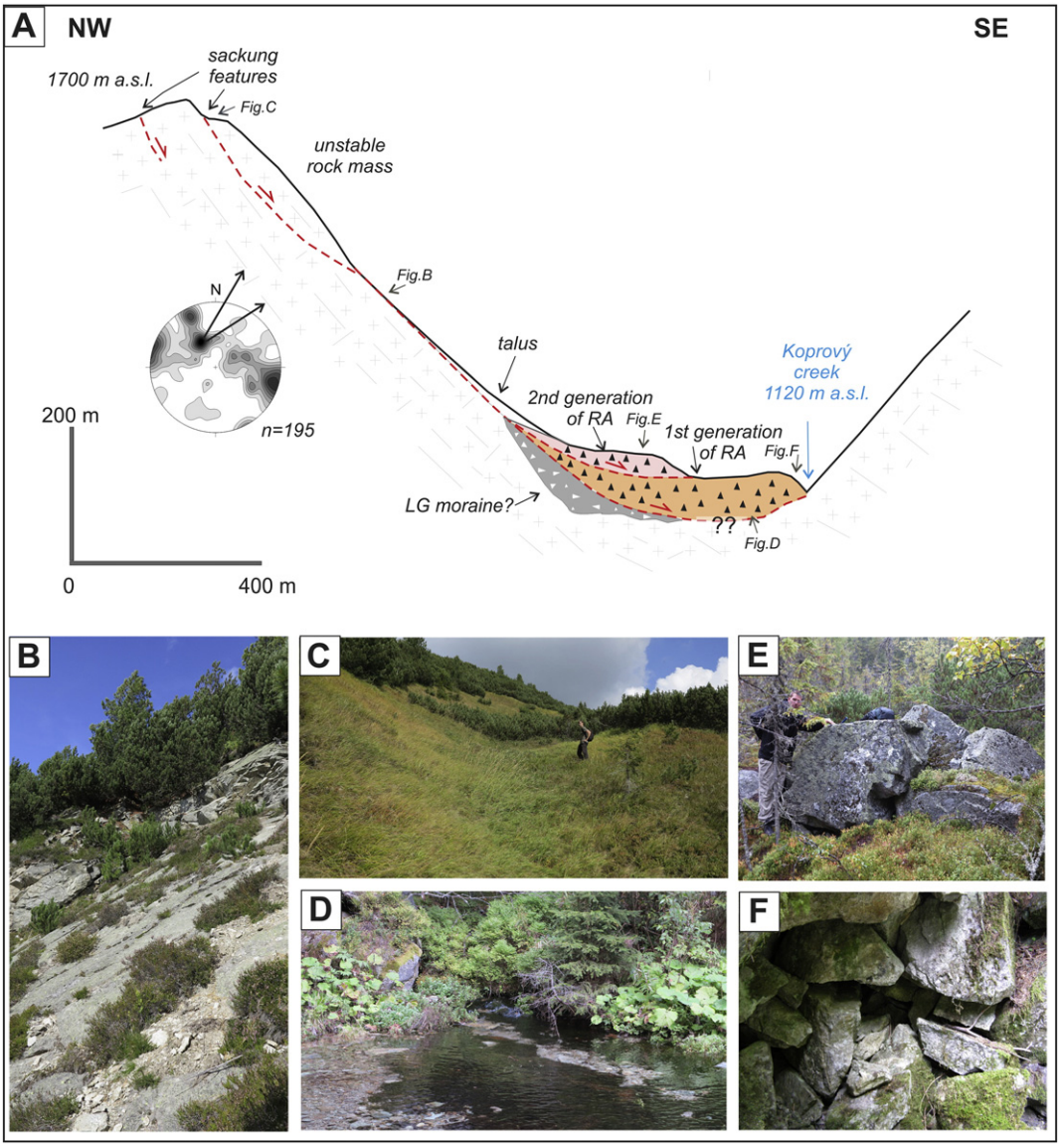

Fig. 5. Polyphase Koprová rock avalanche which once dammed the Kôprovský brook valley (according to drilling, the accumulation thickness overlying the valley floor was more than 40 m) (Lukniš, 1973). A — Cross-section with schematic representation of geological structure (inserted stereonet shows poles of main discontinuity sets in the head scarp area). B — Recent secondary reactivation of rockfall within the head scarp area utilized by slope-parallel joint set. C — Sackung scarp above the head scarp area. D — Outflow of water from the down-valley side of the rock avalanche dam. Significant amount of water from the adjacent Kôprovský brook is infiltrated into the rock avalanche material. E — Large boulders forming carapace of the rock avalanche accumulation. F — Exposure within the boulder/clast-supported accumulation of the rock avalanche.

reveals that the structural and topographic conditions of the Salatín rock avalanche do not favour any simple failure mode (i.e. planar, toppling or wedge type). Only if we assume $\varphi = 20°$, the wedge failure (intersection of pair S4–S5) and flexural toppling (S7) might be possible (Table 2, Fig. 6). The result of the kinematic test for the head scarp of the Koprová rock avalanche is similar to the previous case. There is a small possibility of planar sliding (along K1), wedge failure (K4–K5, $\varphi = 20°$) and flexural toppling (K3), but the percentage of the poles and intersections in the critical zones is very small. If the pre-failure slope gradient was higher than at present, then planar sliding (along K1) would be more probable (Table 2, Fig. 6).

The two kinematically-tested RSFs from the High Tatra Mountains reveal much closer relationships with structural settings and their detachment from the rock massif was likely significantly constrained

Table 2
Percentage of plane poles which falls into critical zone – planar failures and flexural toppling, and percentage of all plane intersections in the critical zone – wedge and direct toppling. Numbers after slash correspond to secondary critical zone.

	Planar		Wedge		Direct toppling		Flexural toppling	
	20°	34°	20°	34°	20°	34°	20°	34°
Salatín	0.14	0.14	5.44/0.21	0.76/0.11	0.57/4.59	4.62/9.69	2.00	1.43
Koprová	2.05	1.54	3.71/1.16	0.47/0.14	1.20/2.22	1.20/5.84	3.08	0.51
Zamkovského	2.38	2.38	7.42/0.86	1.75/0.86	2.74/2.47	2.74/6.84	1.19	1.19
Hrebienok	5.44	5.44	24.59/4.01	20.68/3.98	5.26/4.30	5.26/11.88	6.35	4.54

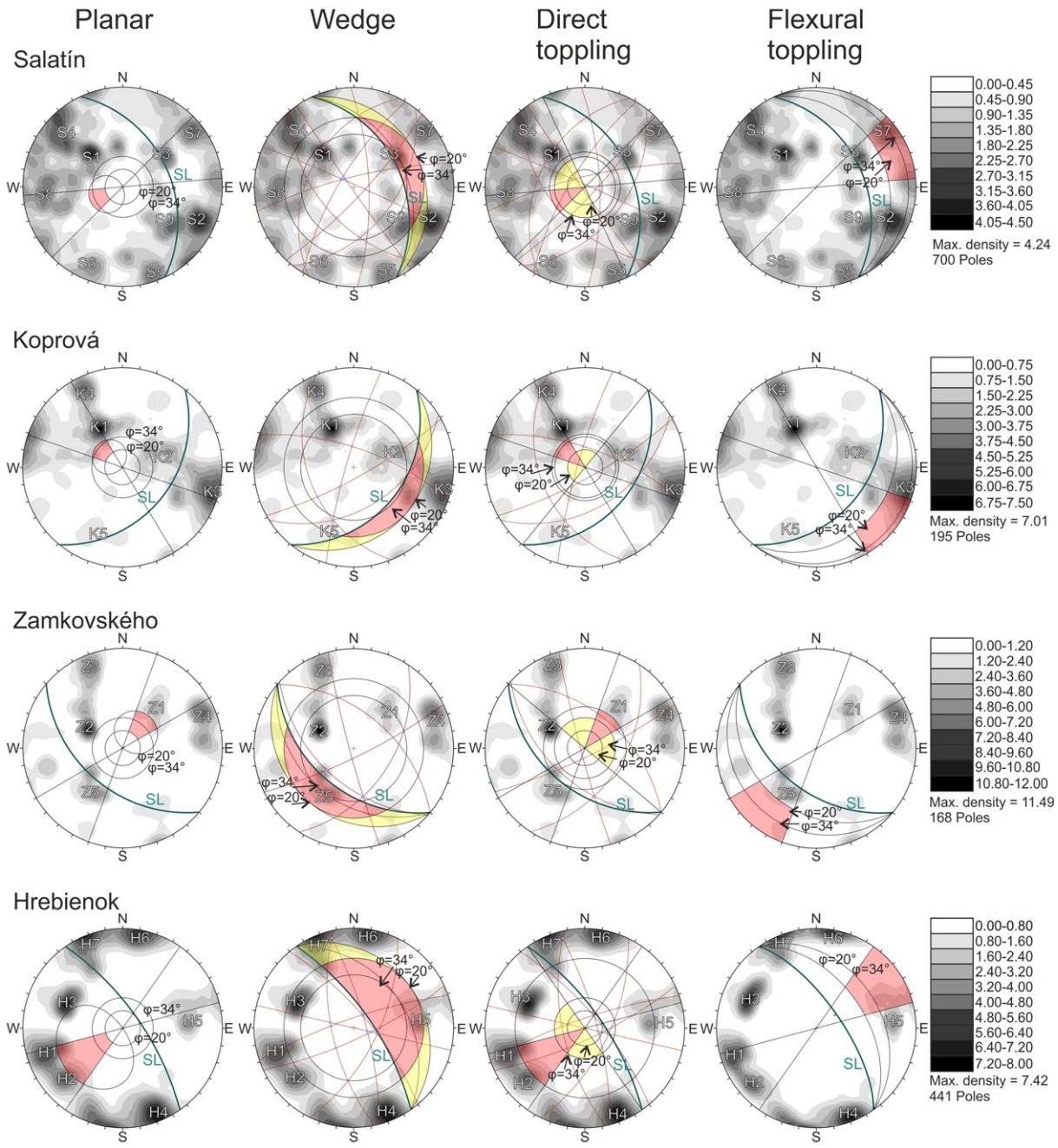

Fig. 6. Kinematic test of selected RSFs. Great circle in blue (SL) corresponds to slope faces. Brown great circles represent mean set planes, their intersections are symbolized by squares. Primary critical zones are presented in the pink area, secondary zone is indicated in yellow. Secondary zone for wedge failure comprises wedges which slide on one joint plane. Secondary zone for direct toppling indicates oblique toppling mode. All plots are equal angle on the lower hemisphere, Fisher contour distribution, counting circle size 1%. Sets are created by the cluster analysis in the Dips 6.0.

by existing discontinuity sets. The Zamkovského rockslide shows a small percentage of poles and intersections in the critical zones. Only a fraction (2.38%) of discontinuities in the set Z1 falls into the critical zone for planar sliding because the dip of these discontinuities is predominantly higher than the dip of the slope. However, if the pre-failure slope gradient was higher (e.g. 60°; which is probable), most of the poles from the Z1 set would fall into the critical zone for planar sliding (Table 2, Fig. 6). Other failure modes appear to be implausible. As for the Hrebienok rockfall, the most probable initial failure mode was a wedge failure (Table 2, Fig. 6). Almost 30% of intersections of all planes lie in the primary and secondary critical zones (for $\varphi = 20°$), for $\varphi = 34°$ it is ~25% of all intersections. The most significant pairs of discontinuity sets which could lead to wedge failure are H3–H7 and H3–H4, intersections of their mean planes are in the critical zone. Also significant are pairs of discontinuities whose intersections of mean planes are near the critical zone. For example ~43% of all intersections of discontinuities from pair H3–H6 fall into the critical zone. The second suitable type of failure is direct toppling, where critical intersection is created by sets H5 and H7. Basal planes are represented by sets H1 and H2, which are also partially suitable for planar sliding. Flexural toppling appears implausible.

Although kinematic testing for Velká Studená and Malá Studená RSFs was not done, it seems from the aerial photographs that both originated (similar to Zamkovského and Hrebienok RSFs) as relatively simple structurally-predisposed failures. The Velká Studená RSF reveals a narrow, corridor-like depletion zone markedly delimited by the

Table 3
Sample sites characteristics and ^{10}Be surface exposure ages.

Sample site	Sample name	Altitude (masl)	Boulder height (m)	Sampled surface dip/aspect (°)	Sample thickness (cm)	Total shielding factor	Production rate (at·g^{-1} yr.$^{-1}$)	^{10}Be concentration (at·g^{-1})	^{10}Be conc. uncertainty (at·g^{-1})	^{10}Be age ± analytical uncertainty (yr)	Weighted mean age (kyr)
Salatín	SalA1	1659	1.0	40/45	2	0.95511	15.636	138,903	5245	8857 ± 334*	10.1 ± 0.3
	SalA2	1661	1.1	13/345	2.5	0.94584	15.444	157,500	6367	10,171 ± 411	
	SalA3	1667	1.0	9/135	3.5	0.94602	15.388	156,080	6505	10,115 ± 422	
Koprová 1	Kopr2	1125	2.0	12/235	4.5	0.94124	10.324	155,287	5439	14,800 ± 518	14.4 ± 0.3
	Kopr3	1135	1.0	28/80	5	0.93350	10.323	147,518	4617	14,100 ± 441	
Koprová 2	Kopr4	1175	1.1	15/45	3	0.94758	10.820	102,041	6596	9522 ± 616	10.2 ± 0.4
	Kopr6	1165	1.3	8/60	3.5	0.92935	10.527	114,713	6443	10,832 ± 608	
Koprová 3	Kopr5	1150	1.5	20/20	2.5	0.93240	10.435	56,461	2936	5219 ± 271	
Velká Studená	SD-27	1613	4.1	11/42	6	0.93887	14.356	214,047	22,227	14,882 ± 1545	15.6 ± 0.7
	SD-28	1618	5.1	Horizontal	4	0.93970	14.663	197,823	33,141	13,463 ± 2255	
	SD-29	1636	3.8	Horizontal	5	0.93893	14.721	210,691	24,380	14,285 ± 1653	
	SD-30	1622	4.2	12/295	3	0.93968	14.823	242,428	15,346	16,333 ± 1034	
	SD-31	1622	4.1	13/312	3	0.93968	14.823	271,868	35,367	18,325 ± 2384	
Malá Studená	MSD-7	1580	3.5	Horizontal	4	0.93508	14.366	229,452	9135	15,955 ± 635	16.5 ± 0.4
	MSD-8	1576	6.0	Horizontal	4	0.93609	14.339	240,717	7208	16,772 ± 502	
Zamkovského	SD-21	1382	5.5	15/180	5	0.95817	12.359	219,028	33,505	17,692 ± 2706	17.0 ± 0.7
	SD-22	1406	4.4	14/180	6	0.95746	12.486	204,994	32,506	16,385 ± 2598	
	SD-23	1409	6.0	Horizontal	2	0.95746	12.938	210,065	13,896	16,206 ± 1072	
	SD-24	1312	4.7	19/150	2	0.96325	12.061	211,518	23,910	17,506 ± 1979	
	SD-25	1312	5.6	15/185	3	0.96343	11.966	210,288	23,794	17,543 ± 1985	
	SD-26	1307	4.3	Horizontal	2	0.96291	12.011	233,506	31,056	19,415 ± 2582	
Hrebienok	SD-16	1227	4.5	4/230	2	0.96055	11.241	257,713	23,538	22,910 ± 2092	20.2 ± 1.2
	SD-17	1231	2.0	6/170	2	0.96062	11.278	207,025	21,485	18,322 ± 1901	
	SD-18	1246	1.3	Horizontal	5	0.95757	11.098	264,821	39,176	23,848 ± 3528	
	SD-19	1242	5.1	5/250	3	0.95831	11.261	131,259	13,702	11,615 ± 1212*	
	SD-20	1223	1.7	22/70	4	0.96582	11.082	199,729	27,039	17,987 ± 2435	

*Sample age excluded from the dataset based on χ^2 test at significance level $\alpha = 0.05$.

intersection of pronounced southward- and northward-dipping discontinuities, which is indicative of a wedge-type failure (Fig. 3). Genesis of the Malá Studená RSF is connected with a slope-parallel joint visible in the head scarp, which likely facilitated a kinematically simple planar failure (Fig. 3).

4.3. Timing of RSFs

Out of the 26 ^{10}Be exposure ages, only three did not pass the χ^2 test performed for individual RSF accumulations, and these samples were rejected from further consideration (Table 3). Uncertainty-weighted mean ages of individual RSF accumulations display, in accordance with geomorphic observations, post-LGM ages ranging between 20.2 ± 1.2 and 10.1 ± 0.3 ka (Table 3, Fig. 7).

^{10}Be exposure ages for three boulders sampled within the Salatín rock avalanche deposit range from 10.2 ± 0.4 ka to 8.9 ± 0.3 ka (Table 3). After exclusion of the youngest exposure age (SalA1; 8.9 ± 0.3 ka) which did not pass the χ^2 test, the weighted arithmetic mean 10.1 ± 0.3 ka of the two remaining boulders approximates to the age of the main rock avalanche depositional event. The early Holocene/Preboreal age of the Salatín rock avalanche is in accordance with geomorphic observations suggesting that slope failure post-dates

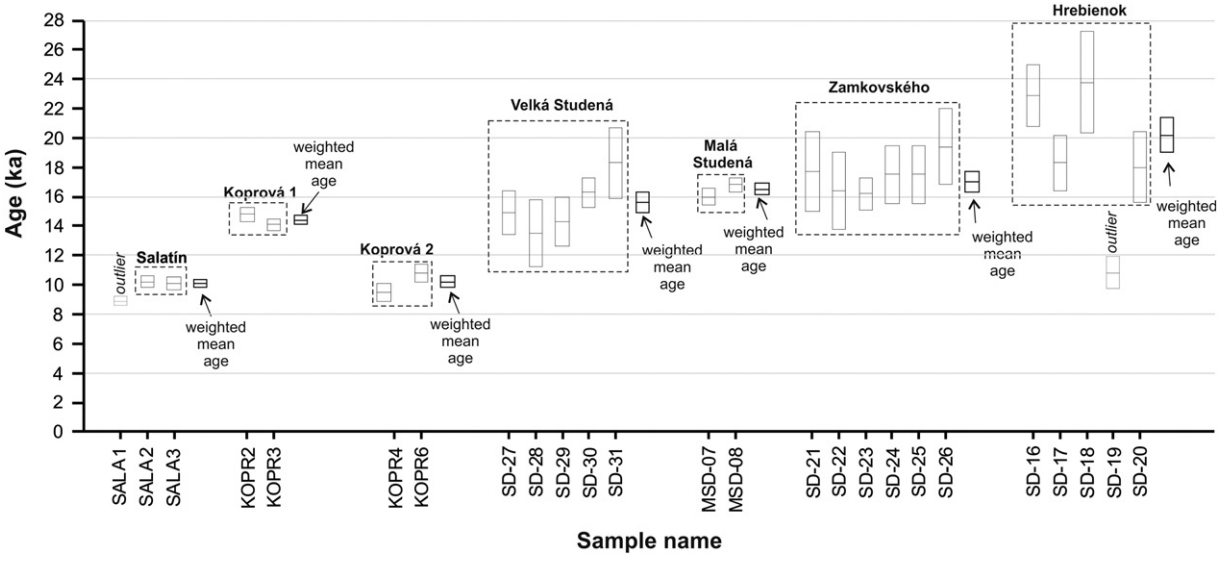

Fig. 7. ^{10}Be and weighted arithmetic mean dates for studied RSFs. Arithmetic means are plotted to the right of the data block for each RSF. Statistical outliers were not used in weighted mean age calculations and are marked in grey.

the origin of the rock glacier covering the valley floor (Figs. 3A and 4A, B).

The dating result is somewhat complex for the Koprová rock avalanche (Table 3, Fig. 7). Five samples taken from the accumulation area yield a relatively high scatter of ages ranging from 14.8 ± 0.5 to 5.2 ± 0.3 ka (Table 3). However, if projected on the geomorphic map (Fig. 3B), the obtained ages fit the morphological peculiarities of the polyphase accumulation. The weighted mean ages of the older and the younger accumulation lobes are 14.4 ± 0.3 and 10.2 ± 0.4 ka respectively (Table 3, Fig. 7). Although the ages of both events are calculated from only two pairs of boulders, the ages in both pairs overlap within the exposure age uncertainty (Fig. 3B). The remaining sample Kopr5 (5.2 ± 0.3 ka) is situated close to the mouth of the secondary chute incising the head scarp and it resulted from a secondary minor rockfall which affected the steep slope above the rock avalanche accumulation. ^{10}Be exposure ages from the Koprová site are consistent with the morphology of the dated accumulation and suggest two distinct RSF events divided by ~4–5 ka time interval.

The oldest group of RSFs is from the highest/eastern part of the Tatra Mountains. The weighted mean ages for Hrebienok, Zamkovského, Velká Studená and Malá Studená RSFs (listed in order of decreasing age) are 20.2 ± 1.2 ka, 17.0 ± 0.7 ka, 16.5 ± 0.4 ka, and 15.6 ± 0.7 ka (Table 3). All of these mean ages are calculated from internally coherent populations of samples which are statistically indistinguishable within particular RSF accumulations at $p < 0.05$ according to the χ^2 test. The only exception was one boulder from the Hrebienok rockfall accumulation (SD19; 11.6 ± 1.2 ka), which revealed too low an age and was rejected as an outlier. The upslope side of this boulder is considerably smaller than its current base which implies that the boulder could have toppled after the rockfall deposition. Although the remaining ($n = 4$) dated boulders within the Hrebienok rockfall accumulation passed the χ^2 test, they still show a higher scatter of ages in comparison with other dated RSFs (Table 3; Fig. 7). Taking into account the complex morphology of both depletion and accumulation areas (e.g. several chutes within the head scarp, multiple longitudinal lobes), we cannot exclude that the Hrebienok rockfall accumulation originated as a result of the sequence of several, chronologically closely-spaced events within the time frame of 10^2–10^3 years (Fig. 7).

5. Discussion

5.1. RSF timing and response to deglaciation

Our study presents the first cosmogenically dated RSFs from the deglaciated mountain ranges of the Carpathians and one of the first case studies in the world where RSF chronology can be correlated with a local high-resolution deglaciation pattern (Cossart et al., 2008; Mercier et al., 2013; Ballantyne et al., 2014a, 2014b). Although there has recently been a growing number of regional landslide chronologies from deglaciated mountains (Prager et al., 2008; Yuan et al., 2013; Moreiras et al., 2015; etc.), these studies usually provide only a temporally low-resolution picture of the response of mass movements to glacier withdrawal, given by the fact that dated RSFs are only seldom situated in the immediate vicinity (e.g. within the same valleys) of dated glacier landforms and deposits. A newly established post-LGM deglaciation chronology for both northern (Makos et al., 2012, 2013) and southern (Makos et al., 2014) slopes of the Tatra Mountains provides a background allowing comparison of RSF timing with the age of glacier withdrawal. Furthermore, the recent study by Engel et al. (2015) provides high-resolution data about the deglaciation of the Velká and Malá Studená dolina Valleys, i.e. the location of four RSFs (Velká Studená, Malá Studená, Zamkovského and Hrebienok) considered in this study (Fig. 8). Although possible earthquake triggers for RSFs cannot be completely ruled out, the seismicity of the Tatra Mountains (and the majority of the Western Carpathians as well) is rather marginal, with historical earthquakes reaching maximum moment magnitudes (M_w) of ~4.5–5.5 (Pagaczewski, 1972). This seismicity level is considered to be the lower boundary for the generation of major rock slope failures (Keefer, 1984). Furthermore, if we take into account that all dated RSFs chronologically well coincide with the deglaciation pattern of the area, we discard seismicity as a possible trigger from the following discussion.

Regarding the chronological response of the studied RSFs to the deglaciation history of the Tatra Mountains, we can distinguish two groups of failures. The first includes RSFs which originated immediately after the glacier retreat (Velká Studená, Malá Studená, Zamkovského and Hrebienok), and the second group includes failures which were delayed by several millennia in respect to the deglaciation of particular valley sections (Salatín and Koprová RSFs). RSFs in the eastern part of the mountains within the Velká and Malá Studená dolina Valleys postdate the local LGM (herein determined to ~22 ka; Engel et al., 2015) and their ages decrease in the up-valley direction, corresponding to glacier retreat (Fig. 8). The oldest/lowest RSF (Hrebienok) age ~20.2 ka is close to the LGM terminal moraine, whereas the youngest one (Velká Studená) is located high in the trough and is dated to ~15.6 ka; two intervening RSFs (Zamkovského and Malá Studená) reveal ages 17.0 and 16.5 ka (Fig. 8). In comparison with the ages of the nearest down-valley dated glacial features and regarding the calculated glacier retreat rates (Engel et al., 2015), most of these RSFs took place a few hundred years after the glacier retreat from particular sections of the troughs

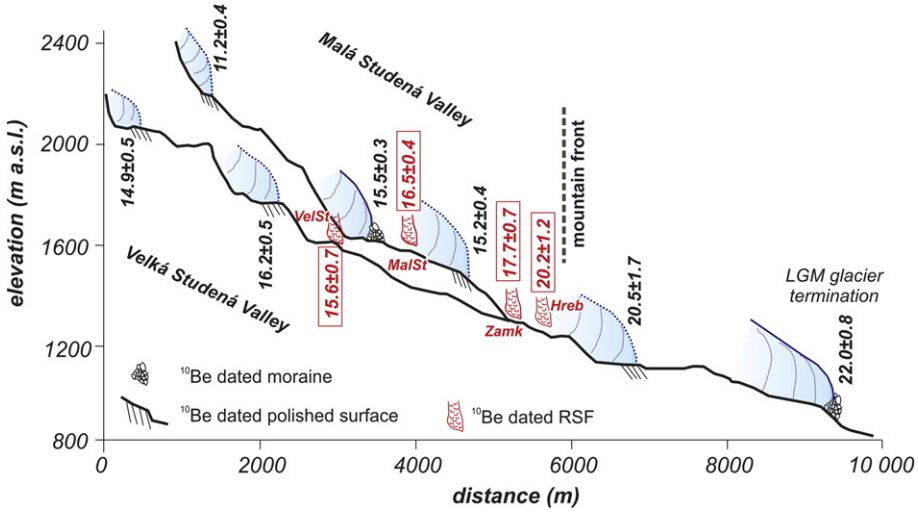

Fig. 8. Timing of RSFs and deglaciation (after Engel et al. (2015)) of the Velká and Malá Studená Valleys plotted in the longitudinal profiles of valleys.

Table 4
Overview of chronological studies where paraglacial conditions are discussed among factors contributing to the genesis of prehistoric catastrophic RSFs.

Study	Region	Dataset	Dating method	Age of RSFs	Time lag of RSFs following deglaciation	Probable role of paraglaciation[1]
Orwin et al. (2004)	British Columbia/Canada	Cheam rock avalanche with volume ~0.18 km^3	^{14}C	~5 ka	~6 ka	Preparatory factor
Sturzenegger et al. (2015)	Canadian Rocky Mountains	Palliser recurrent rockslides with volumes ~40 Mm^3 and ~8 Mm^3 respectively	^{36}Cl	~10 ka followed by younger one at ~7.7 ka	~3 ka	Preparatory factor
Stock and Uhrhammer (2010)	Yosemite Valley/California-USA	El Captain rock avalanche with volume ~2.2 Mm^3	^{10}Be	~3.6 ka	~13 ka	Preparatory factor
Fauqué et al. (2009); Hermanns and Longva (2012)	Central Andes/Argentina	13 rock avalanches in the Cerro Acocangua region	^{14}C and ^{36}Cl	~18–4.1 ka	Except for two cases, majority of RSFs collapsed immediately or with the time lag of max. few ka	Both preparatory and triggering factor
Mercier et al. (2013)	Skagafjördur area/Iceland	Höfðahólar rock avalanche	^{14}C	~9–8.2 ka	>3.8 ka	Triggering factor-seismicity related to postglacial rebound
Blikra et al. (2006)	Troms County/northern Norway	Grøtura, Fornes and Russeneset rock avalanches	^{14}C	~11.5–10.6 ka	immediately or with the time lag of max. few ka	Triggering factor only for few oldest rock avalanches
Schleier et al. (2015)	Innerdalen/Western Norway	Skarfjellet recurrent rock avalanches with volumes 31 Mm^3 and 23 Mm^3 respectively	^{10}Be	~14.1 ka followed by younger one at ~8.0 ka	Older event took place just before deglaciation (emplacement on glacier surface)	Triggering factor for older event
Ballantyne et al. (2014a)	Scotland and Northern Ireland	31 RSFs with maximum volume ~3 Mm^3	^{10}Be and ^{36}Cl	18.2–1.2 ka	95% of RSFs originated ~5400 years after deglaciation, with peak RSF activity 1600–1700 years after deglaciation	Triggering factor - majority of RSFs caused by seismicity related to postglacial rebound
Soldati et al. (2004)	Dolomites/Italian Alps		^{14}C	~15.7–0.7 ka	Oldest events are nearly coeval with deglaciation which took place 14–11 ka	Triggering factor only for few oldest rockslides
Van Husen et al. (2007)	Calcareous Alps/Austria	~0.45 km^3 Almtal rock avalanche	^{36}Cl	~19 ka followed by younger one at ~15.6 ka	First event is coeval with LGM deglaciation	Triggering factor
Cossart et al. (2008)	Upper Durance catchment/French Alps	The Pré de Madame Carle rock avalanche (~1–10 Mm^3)	^{10}Be	~10 ka followed by younger one at ~1.5 ka	First event is coeval with deglaciation	Triggering factor
Hormes et al. (2008)	Alta Valtellina/Italian Alps	Val Viola rock avalanche	^{10}Be	~7.4 ka	~4 ka	Preparatory factor
Prager et al. (2008)	Tyrol/Eastern Alps	Compilation of 47 dated RSFs	^{14}C,^{36}Cl, ^{10}Be	~15.5–0.5 ka	Except of one event coeval with glacier withdrawal, other RSFs originated at least 1–2 ka after deglaciation	Preparatory factor
Ivy-Ochs et al. (2009)	Graubünden/Swiss Alps	~12 km^3 Flims rock avalanche	^{36}Cl and ^{10}Be	~8.9 ka	>4.4 ka	Preparatory factor[2]
Claude et al. (2014)	Valle Levantina/Swiss Alps	~0.53 km^3 Chironico rockslide	^{36}Cl	~13 ka	~3 ka	Preparatory factor
Hughes et al. (2014)	High Atlas/Morocco	Arroumd rock avalanche	^{10}Be	~4.5 ka	~7 ka	Preparatory factor
Shroder et al. (2011)	Karakoram/Pakistan	Ghoro Choch (0.4 km^3) and Gomboro (0.1 km^3) rock avalanches	^{10}Be	~15.8–9.2 ka	Both rock avalanches collapsed immediately or with a time lag of max. few ka	Triggering factor
Dortch et al. (2009)	Himalaya/India	Four rock avalanches with volumes between ~0.01–0.52 km^3	^{10}Be	~8.5–6.5 ka	~2–4 ka	Preparatory factor
Hancox and Perrin (2008)	Fiordland/New Zealand	~26 km^3 Green Lake rockslide	^{14}C	~13–12.5 ka	~1–1.5 ka	Preparatory factor
Sweeney et al. (2013)	Fiordland/New Zealand	~0.7 km^3 Lochnagar rockslide	^{10}Be	~9 ka	~5 ka	Preparatory factor

[1] Preparatory factors involve especially debutressing, glacial erosion, sheet jointing, static fatigue and some climatic influences. As for the triggering factors, most likely are debutressing, sheet jointing, seismicity related to post-glacial rebound and climatic effects (McColl, 2012).
[2] RSF is nearly coeval with two nearby situated giant Köfels (9.8 ka; 3.3 km^3) and Kandertal (9.6 ka; 0.8 km^3) rock avalanches.

(Fig. 8). Therefore, among hitherto published cases of dated paraglacial RSFs (e.g. Soldati et al., 2004; Cossart et al., 2008; Prager et al., 2008; Mercier et al., 2013; Ballantyne et al., 2014a, 2014b), our results from the Velká and Malá Studená dolina Valleys represent quite rare examples of a nearly immediate response by RSFs to ice retreat (Table 4).

As demonstrated by Prager et al. (2008) and Ballantyne et al. (2014a, 2014b), the majority of paraglacial RSFs respond to glacier retreat with a millennial time lag, revealing the long-term nature of stress relaxation within the rock mass and/or delayed crustal rebound and accompanied seismic activity due to the isostatic uplift of deglaciated terrains. It seems that our discussed examples from the eastern part of the Tatra Mountains do not fit this scenario and originated directly either due to the loss of glacier ice support and related debutressing or paraglacial fracturing of oversteepened rock walls, i.e. their trigger was directly related to paraglacial processes (compare e.g. McColl, 2012). In comparison with other European mountains (e.g. the Scottish Highlands, European Alps, Scandinavian Mountains) where a substantial number of RSFs post-date Younger Dryas (12.9–11.7 b2k, Rasmussen et al., 2014), major RSFs in the eastern part of the Tatra Mountains predate this period due to the limited extent of glaciers which occupied only the uppermost parts of glacial troughs and cirques within the Younger Dryas (Engel et al., 2015).

Although two dated RSFs (Salatín and Koprová) in the Western Tatra Mountains are not supported by local deglaciation chronology, their location in glacier valleys close to the High Tatra Mountains allows for tentative timing of RSFs (Fig. 1; Makos et al., 2012, 2013, 2014). As for the Koprová rock avalanche, it originated close to the LGM terminal moraine of the Kôprovský potok Valley. Terminal moraines of the nearby Mlynická and Velická dolina Valleys were stabilized according to Makos et al. (2014) between 20 and 18 ka ago, therefore if we take into account the age of the first rock avalanche event of the Koprová RSF (~14.4 ka), it originated at least ~4–6 ka following the glacier withdrawal. The second rock avalanche event (~10.2 ka), which took place in the same source area, post-dated the presence of a glacier by more than ~8–10 ka. Estimation of the time lag for the Salatín rock avalanche which collapsed from the cirque headwall in the uppermost part of the valley is more uncertain. However, if we assume that this area was occupied by a small glacier during the Younger Dryas period, the delay of RSF was ~1 ka, considering that the final deglaciation of similar positions in other parts of the Tatra Mountains is dated to ~11 ka (Makos et al., 2012; Engel et al., 2015).

The pronounced time lag of these three RSF events following deglaciation in the Western Tatra Mountains suggests that these collapses were not directly driven by paraglacial stress release. Although glacial processes prepared the topography for subsequent collapses, their triggers were likely related to climatic factors (Soldati et al., 2004; Prager et al., 2008), or alternatively RSFs originated due to the progressive weakening of the rock mass (Hancox et al., 1999; McColl, 2012). Rock avalanche events in the Koprová site and the Salatín rock avalanche can be well correlated with major climatic changes. The first Koprová rock avalanche (~14.4 ka) postdates the beginning of regional warming ~15 ka, correlating with the onset of the Bølling–Allerød chronozone (Blockley et al., 2012; Lischke et al., 2013). Similarly, the second Koprová rock avalanche (~10.2 ka) and the Salatín rock avalanche (~10.1 ka) probably followed the onset of the Holocene (suggested as abrupt warming at 11,320 b2k – Kobashi et al., 2008; Rasmussen et al., 2014) (Fig. 9). Both climate deteriorations are documented by proxy data in Central Europe, such as pollen (Feurdean et al., 2014), speleothem (Hercman, 2000) or fluvial (Starkel et al., 2006) records, supporting the existence of a warmer and more humid climate in the Western Carpathians. Besides hydrometeorological extremes, these rock avalanche events might also be triggered by permafrost degradation, presumably accelerated during warmer climatic conditions (McColl, 2012; Claude et al., 2014). Minor instabilities (e.g., small rockfalls and debris flows) from steep head scarps have likely continued for the whole Holocene, which is evidenced also by two negative anomalies (too young boulders) in our dataset.

5.2. Volume, structural settings, terrain conditions and genesis of RSFs

Despite the high quantity of slow-moving, deep-seated gravitational slope deformations in the Western Tatra Mountains (Němčok, 1982), catastrophic RSFs in the Tatra Mountains are relatively scarce in comparison with other high mountain areas and reach only a limited size. Although Lukniš (1973) estimated the volume of the largest RSF in the area (the Koprová rock avalanche) as ~8×10^6 m^3, our result suggests a more limited volume of ~5.4×10^6 m^3 (Table 1). Even this, the largest RSF in the Tatra Mts., is at least an order of magnitude smaller than the largest RSFs documented in topographically similar mountains, including the Northern Calcareous Alps (Prager et al., 2008), Apennines (Bianchi Fasani et al., 2014), Pyrenees (Jarman et al., 2014) and Scandinavian Mountains (Blikra et al., 2006). The main reason is the predominance of granitoid rocks in the Tatra Mountains, which are characterized by overall high rock mass strength (Selby, 1993). The scarcity of RSFs within granitoid domains has also been reported from other mountain areas (Crosta et al., 2013; Ballantyne et al., 2014a, 2014b; Jarman et al., 2014). Therefore it is not surprising that major RSFs in the Tatra Mountains are concentrated in zones of substantially weakened rock mass, such as major tectonic faults (Koprová, Zamkovského and Hrebienok RSFs), slopes deformed by long-term deep-seated creep (Salatín and Koprová RSFs), or originated on exposed kinematically feasible discontinuity sets and their intersections (Velká Studená and Malá Studená RSFs).

The structural settings and geomorphic positions of individual RSFs likely influenced their chronological responses to glacier retreat. RSFs with immediate responses to deglaciation are situated in the highest and steepest parts of the Tatra Mountains, where slopes are probably close to their threshold conditions (Fig. 2). According to the "threshold hillslopes" concept (Montgomery, 2001), even a slight change of slope geometry (esp. steepening, increasing slope height, etc.) leads to fast landsliding and establishment of new stability. The abrupt reaction of rock slopes to changed stability conditions in the highest parts of the Tatra Mountains was additionally facilitated by the presence of kinematically feasible discontinuity sets which were exposed by glacier erosion. Resulting slope failures were thereafter detached as kinematically relatively simple failures (planar, wedge or toppling) and in most cases collapsed as rockfalls. The delayed RSFs from the Western Tatra Mountains are situated in different topographic settings, with gentler hillslopes and their relationship with the bedrock structure is more complex. Furthermore, both RSFs have their source areas situated within deep-seated gravitational slope deformations, which indicate prolonged stress relaxation within the rock massif and perhaps a recurrent nature of slope failures (see e.g. Böhme et al. (2013); Barth (2014)).

6. Conclusion

Cosmogenic age constraints on major RSFs in the Tatra Mountains show that slope collapses originated in close coincidence with paraglacial conditions following the Late Pleistocene deglaciation. Weighted mean ages of RSFs range between 20.2 ± 1.2 and 10.1 ± 0.3 ka. Nevertheless, the time response of an individual RSF in respect to the withdrawal of glaciers, and thus the mechanisms of how ice retreat influenced the instability of rock slopes, was rather complex. RSFs situated in the threshold-hillslope domain of the highest part of the mountains originated mostly a few hundred years after the deglaciation of particular valley sections, implying that glacially-conditioned stress release (debutressing, paraglacial fracturing, etc.) was probably the main factor of slope instabilities. The immediate response of such failures was likely facilitated by local structural predisposition and relatively simple kinematics. The cases described from the western part of the mountains (involving the largest event, ~5.4×10^6 m^3 Koprová

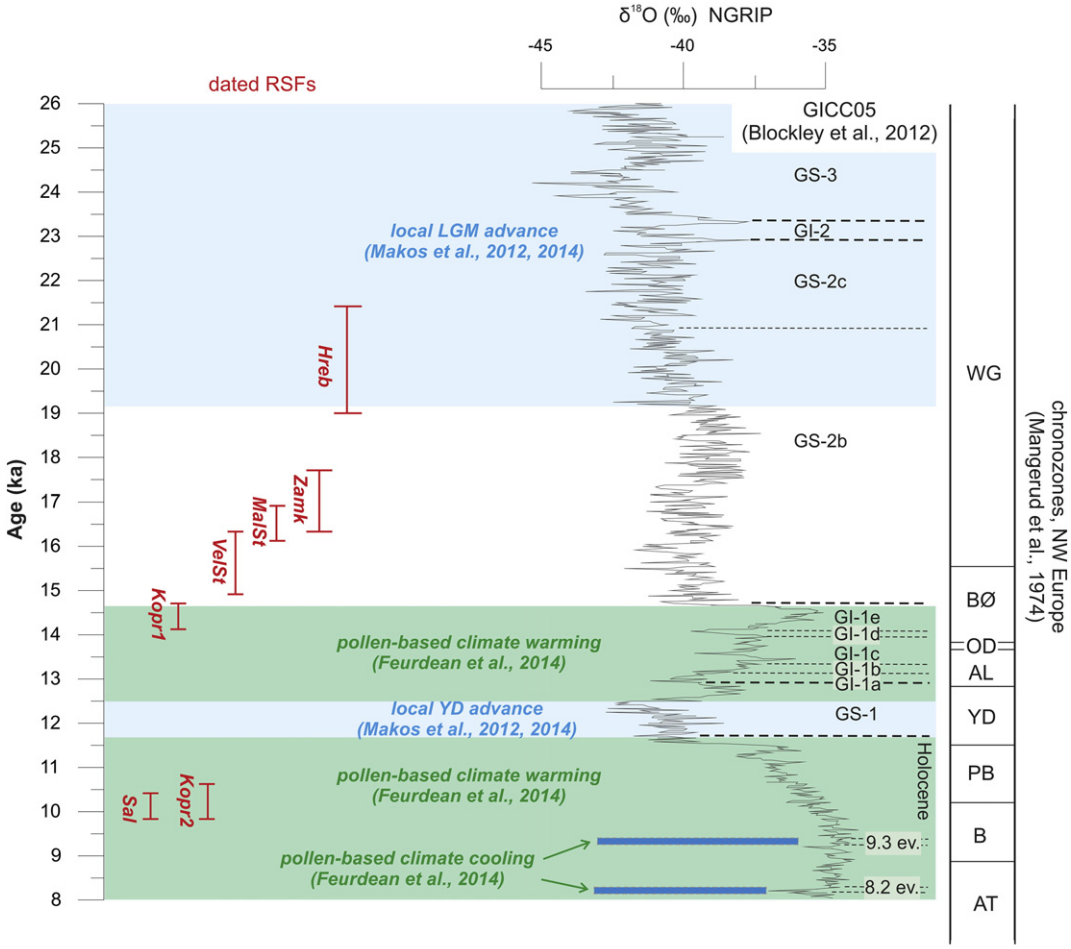

Fig. 9. Timing of studied RSFs expressed by weighted mean ages and their chronological context against NorthGRIP $\delta^{18}O$ record originally published by North Greenland Ice Core Project members (2004) and selected regional paleoenvironmental proxies. Chronozones in NW Europe according to Mangerud et al. (1974).

rock avalanche) situated within gentler topography and coinciding with deep-seated gravitational slope deformations, reveal a pronounced millennial-scale time lag following ice retreat. In such cases, deglaciation did not represent an immediate factor for catastrophic failures, but only prepared the rock slopes for further destabilizations, which most likely accentuated the role of the climate. As demonstrated by the Koprová polyphase rock avalanche, both collapses originated during the warm and humid periods of the Bølling–Allerød chronozone and after the onset of the Holocene. Although limited in size, our dataset of ^{10}Be-dated RSFs is correlated with the unique high-resolution deglaciation history of the mountain range and thus provides an important contribution to the recent discussion about the paraglacial responses of rock slopes.

Acknowledgements

This study was conducted within the framework of the Czech Science Foundation, project 13-15123S. The authors would like to thank J. King of the University of West Bohemia for providing language help. The suggestions of two anonymous reviewers also helped to improve the quality of this paper.

References

Allen, S.K., Cox, S.C., Owens, I.F., 2011. Rock avalanches and other landslides in the central Southern Alps of New Zealand: a regional study considering possible climate change impacts. Landslides 8, 33–48.

Arnold, M., Merchel, S., Bourlès, D.L., Braucher, R., Benedetti, L., Finkel, R.C., Aumaître, G., Gottdang, A., Klein, M., 2010. The French accelerator mass spectrometry facility ASTER: improved performance and developments. Nucl. Instrum. Methods Phys. Res., Sect. B 268, 1954–1959.

Balco, G., Briner, J., Finkel, R.C., Rayburn, J.A., Ridge, J.C., Schaefer, J.M., 2009. Regional beryllium-10 production rate calibration for late-glacial northeastern North America. Quat. Geochronol. 4 (2), 93–107.

Ballantyne, C.K., 2002. Paraglacial geomorphology. Quat. Sci. Rev. 21, 1935–2017.

Ballantyne, C.K., Wilson, P., Schnabel, C., Xu, S., 2013. Lateglacial rock slope failures in north-west Ireland: age, causes and implications. J. Quat. Sci. 28, 789–802.

Ballantyne, C.K., Sandeman, G.F., Stone, J.O., Wilson, P., 2014a. Rock-slope failure following Late Pleistocene deglaciation on tectonically stable mountainous terrain. Quat. Sci. Rev. 86, 144–157.

Ballantyne, C.K., Wilson, P., Gheorghiu, D., Rodés, Á., 2014b. Enhanced rock-slope failure following ice-sheet deglaciation: timing and causes. Earth Surf. Process. Landf. 39, 900–913.

Barth, N.C., 2014. The Cascade rock avalanche: implications of a very large Alpine Fault-triggered failure, New Zealand. Landslides 11, 327–341.

Bianchi Fasani, G., Di Luzio, E., Esposito, C., Evans, S.G., Scarascia Mugnozza, G., 2014. Quaternary, catastrophic rock avalanches in the central Apennines (Italy): relationships with inherited tectonic features, gravity-driven deformations and the geodynamic frame. Geomorphology 211, 22–42.

Blikra, L.H., Longva, O., Braathen, A., Dehls, J.F., Stalsberg, K., 2006. Rock Slope Failures in Norwegian Fjord Areas: Examples, Spatial Distribution and Temporal Pattern. In: Evans, S.G., Mugnozza, G.S., Strom, A., Hermanns, R.L. (Eds.), Landslides from Massive Rock Slope Failure. Springer, Dordrecht, pp. 475–496.

Blockley, S.P.E., Lane, C.S., Hardiman, M., Rasmussen, S.O., Seierstad, I.K., Steffensen, J.P., Svensson, A., Lotter, A.F., Turney, C.S.M., Ramsey, C.B., INTIMATE members, 2012. Synchronisation of palaeoenvironmental records over the last 60,000 years, and an extended INTIMATE event stratigraphy to 48,000 b2k. Quat. Sci. Rev. 36, 2–10.

Böhme, M., Hermanns, R.L., Oppikofer, T., Fischer, L., Bunkholt, H.S.S., Eiken, T., Pedrazzini, A., Derron, M.H., Jaboyedoff, M., Blikra, L.H., Nilsen, B., 2013. Analyzing complex rock slope deformation at Stampa, western Norway, by integrating geomorphology, kinematics and numerical modeling. Eng. Geol. 154, 116–130.

Braucher, R., Merchel, S., Borgomano, J., Bourlès, D.L., 2011. Production of cosmogenic radionuclides at great depth: a multi element approach. Earth Planet. Sci. Lett. 309 (1–2), 1–9.

Brideau, M.A., Stead, D., Couture, R., 2006. Structural and engineering geology of the East Gate Landslide, Purcell Mountains, British Columbia. Eng. Geol. 84, 183–206.

Brideau, M.A., Pedrazzini, A., Stead, D., Froese, C., Jaboyedoff, M., van Zeyl, D., 2011. Three-dimensional slope stability analysis of South Peak, Crowsnest Pass, Alberta, Canada. Landslides 8, 139–158.

Briner, J.P., Young, N.E., Goehring, B.M., Schaefer, J.M., 2012. Constraining Holocene Be production rates in Greenland. J. Quat. Sci. 27 (1), 2–6.

Chmeleff, J., von Blanckenburg, F., Kossert, K., Jakob, D., 2010. Determination of the Be half-life by multicollector ICP-MS and liquid scintillation counting. Nucl. Instrum. Methods Phys. Res., Sect. B 263 (2), 192–199.

Clark, P.U., Dyke, A.S., Shakun, J.D., Carlson, A.E., Clark, J., Wohlfarth, B., Mitrovica, J.X., Hostetler, S.W., McCabe, A.M., 2009. The Last Glacial Maximum. Science 325, 710–714.

Claude, A., Ivy-Ochs, I., Kober, F., Antognini, M., Salcher, B., Kubik, P.W., 2014. The Chironico landslide (Valle Leventina, southern Swiss Alps): age and evolution. Swiss J. Geosci. 107, 273–291.

Cossart, É., Braucher, R., Fort, M., Bourlès, D.L., Carcaillet, J., 2008. Slope instability in relation to glacial debuttressing in Alpine areas (Upper Durance catchment, southeastern France): evidence from field data and ^{10}Be cosmic ray exposure ages. Geomorphology 95, 3–26.

Cossart, É., Mercier, D., Decaulne, A., Feuillet, T., Jónsson, H.P., Sæmundsson, Þ., 2014. Impacts of post-glacial rebound on landslide spatial distribution at a regional scale in Northern Iceland (Skagafjörður). Earth Surf. Process. Landf. 39, 336–350.

Crosta, G., Frattini, P., Agliardi, F., 2013. Deep seated gravitational slope deformations in the European Alps. Tectonophysics 605, 13–33.

Cruden, D., Hu, X.Q., 1993. Exhaustion and steady state models for predicting landslide hazards in the Canadian Rocky Mountains. Geomorphology 8, 279–285.

Cruden, D.M., Varnes, D.J., 1996. Landslide types and processes. In: Turner, A.K., Schuster, R.L. (Eds.), Landslides Investigation and Mitigation. Transportation Research Board, US National Research Council. Special Report 247, Washington, DC, pp. 36–75.

Dortch, J., Owen, L.A., Haneberg, W.C., Caffee, M.W., Dietsch, C., Kamp, U., 2009. Nature and timing of mega-landslides in northern India. Quat. Sci. Rev. 28, 1037–1054.

Dunne, J., Elmore, D., Muzikar, P., 1999. Scaling factors for the rates of production of cosmogenic nuclides for geometric shielding and attenuation at depth on sloped surfaces. Geomorphology 27 (1–2), 3–11.

Engel, Z., Mentlík, P., Braucher, R., Minár, J., Léanni, L., Team Aster, 2015. Geomorphological evidence and ^{10}Be exposure ages for the Last Glacial Maximum and deglaciation of the Velká and Malá Studená dolina Valleys in the High Tatra Mountains. Quat. Sci. Rev. 124, 106–123.

Fauqué, L., Hermanns, R., Hewitt, K., Rosas, M., Wilson, C., Baumann, V., Lagorio, S., Di Tommaso, I., 2009. Mega-deslizamientos de la pared sur del Cerro Aconcagua y su relación con depósitos asignados a la glaciación pleistocena. Rev. Asoc. Geol. Argent. 65, 691–712.

Fenton, C.R., Hermanns, R.L., Blikra, L.H., Kubik, P.W., Bryant, C., Niedermann, S., Meixner, A., Goethals, M.M., 2011. Regional Be production rate calibration for the past 12 ka deduced from the radiocarbon-dated Grøtlandsura and Russenes rock avalanches at 69 N. Quat. Geochronol. 6 (5), 437–452.

Feurdean, A., Perşoiu, A., Tanţău, I., Stevens, T., Magyari, E.K., Onac, B.P., Marković, S., Andrič, M., Connor, S., Fărcaş, S., Gałka, M., Gaudeny, T., Hoek, W., Kolaczek, P., Kuneš, P., Lamentowicz, M., Marinova, E., Michczyńska, D.J., Perşoiu, I., Płóciennik, M., Słowiński, M., Stancikaite, M., Sumegi, P., Svensson, A., Tămaş, T., Timar, A., Tonkov, S., Toth, M., Veski, S., Willis, K.J., Zernitskaya, V., 2014. Climate variability and associated vegetation response throughout Central and Eastern Europe (CEE) between 60 and 8 ka. Quat. Sci. Rev. 106, 206–224.

Goehring, B.M., Lohne, Ø.S., Mangerud, J., Svendsen, J.I., Gyllencreutz, R., Schaefer, J., Finkel, R., 2012. Late Glacial and Holocene beryllium-10 production rates for western Norway. J. Quat. Sci. 27 (1), 89–96.

Hancox, G.T., Perrin, N.D., 2008. Green Lake Landslide and other giant and very large post-glacial landslides in Fiordland. Quat. Sci. Rev. 28, 1020–1036.

Hancox, G.T., McSaveney, M.J., Davies, T.R., Hodgson, K., 1999. Mt. Adams rock avalanche of 6 October 1999 and subsequent formation and breaching of a large landslide dam in Poerua River, Westland, New Zealand. Institute of Geological & Nuclear Sciences Science Report 99/19 (Lower Hutt, 22 pp.).

Hercman, H., 2000. Reconstruction of palaeoclimatic changes in Central Europe between 10 and 200 thousand years BP, based on analysis of growth frequency of speleothems. Studia Quaternaria 17, 35–70.

Hermanns, R.L., Longva, O., 2012. Rapid Rock-Slope Failures. In: Clague, J.J., Stead, D. (Eds.), Landslides: Types, Mechanisms and Modeling. Cambridge University Press, Cambridge, pp. 59–70.

Hermanns, R.L., Niedermann, S., Villanueva, A., Sosa Gomez, J., Strecker, M.R., 2001. Neotectonics and catastrophic failure of mountain fronts in the southern intra-Andean Puna Plateau. Geology 29, 619–623.

Hewitt, K., 1999. Quaternary Moraines vs Catastrophic Rock Avalanches in the Karakoram Himalaya, Northern. Quat. Res. 51, 220–237.

Hewitt, K., Gosse, J., Clague, J.J., 2011. Rock avalanches and the pace of late Quaternary development of river valleys in the Karakoram Himalaya. Geol. Soc. Am. Bull. 123, 1836–1850.

Holm, K., Bovis, M., Jakob, M., 2004. The landslide response of alpine basins to post-Little Ice Age glacial thinning and retreat in southwestern British Columbia. Geomorphology 57, 201–216.

Hormes, A., Ivy-Ochs, S., Kubik, P.W., Ferreli, L., Maria Michetti, A., 2008. ^{10}Be exposure ages of rock avalanche and a late glacial moraine in Alta Valtellina, Italian Alps. Quat. Int. 190, 136–145.

Hsü, K.J., 1975. Catastrophic debris streams (sturzstroms) generated by rockfalls. Geol. Soc. Am. Bull. 86, 129–140.

Hughes, P.D., Fink, D., Fletcher, W.J., Hannah, G., 2014. Catastrophic rock avalanches in a glaciated valley of the High Atlas, Morocco: ^{10}Be exposure ages reveal a 4.5 ka seismic event. Geol. Soc. Am. Bull. 126, 1093–1104.

Hungr, O., Evans, S.G., Bovis, M.J., Hutchinson, J.N., 2001. A review of the classification of landslides of the flow type. Environ. Eng. Geosci. 7, 221–238.

Hungr, O., Leroueil, S., Picarelli, L., 2014. The Varnes classification of landslide types, an update. Landslides 11, 167–194.

Ivy-Ochs, S., von Poschinger, A., Synal, H.A., Maisch, M., 2009. Surface exposure dating of the Flims landslide, Graubünden, Switzerland. Geomorphology 103, 104–112.

Jarman, D., Calvet, M., Corominas, J., Delmas, M., Gunnell, Y., 2014. Large-scale rock slope failures in the Eastern Pyrenees: identifying a sparse but significant population in paraglacial and parafluvial contexts. Geogr. Ann. A 96, 357–391.

Kalvoda, J., 1994. Rock slopes of the High Tatras Mountains. Acta Univ. Carol. Geol. 29, 13–33.

Keefer, D.K., 1984. Landslides caused by earthquakes. Geol. Soc. Am. Bull. 95, 406–421.

Kłapyta, P., 2013. Application of Schmidt hammer relative age dating to Late Pleistocene moraines and rock glaciers in the Western Tatra Mountains, Slovakia. Catena 111, 104–121.

Kobashi, T., Severinghaus, J.P., Barnola, J.M., 2008. 4 ± 1.5 C abrupt warming 11,270 yr ago identified from trapped air in Greenland ice. Earth Planet. Sci. Lett. 268, 397–e407.

Korschinek, G., Bergmaier, A., Faestermann, T., Gerstmann, U.C., Knie, K., Rugel, G., Wallner, A., 2010. A new value for the half-life of Be by heavy-ion elastic recoil detection and liquid scintillation counting. Nucl. Instrum. Methods Phys. Res., Sect. B 268 (2), 187–191.

Korup, O., Densmore, A.L., Schlunegger, F., 2010. The role of landslides in mountain range evolution. Geomorphology 120, 77–90.

Kotarba, A., Długosz, M., 2010. Alpine cliff evolution and debris flow activity in the High Tatra Mountains. Stud. Geomoph. Carpatho-Balcan. 44, 35–47.

Králiková, S., Vojtko, R., Sliva, L., Minár, J., Fugenschuh, B., Kováč, M., Hók, J., 2014. Cretaceous–Quaternary tectonic evolution of the Tatra Mts (Western Carpathians): constraints from structural, sedimentary, geomorphological, and fission track data. Geol. Carpath. 65, 307–326.

Lebourg, T., Zerathe, S., Fabre, R., Giuliano, J., Vidal, M., 2014. A Late Holocene deep-seated landslide in the northern French Pyrenees. Geomorphology 208, 1–10.

Lischke, H., von Grafenstein, U., Ammann, B., 2013. Forest dynamics during the transition from the Oldest Dryas to the Bølling–Allerød at Gerzensee—a simulation study. Palaeogeogr. Palaeoclimatol. Palaeoecol. 391, 60–73.

Longva, O., Blikra, L.H., Dehls, J.F., 2009. Rock avalanches: distribution and frequencies in the inner part of Storfjorden, Møre og Romsdal County, Norway. Geological Survey of Norway, p. 32. Report 2009.002.

Lukniš, M., 1968. Geomorphological Map of the Vysoké Tatry Mts. (High Tatra Mts.) and their Foreland 1:50,000. Geologický ústav Dionýza Štúra, Bratislava.

Lukniš, M., 1973. Reliéf Vysokých Tatier a ich predpolia. Veda, Bratislava.

Mahr, T., Němčok, A., 1977. Deep-seated creep deformations in the crystalline cores of the Tatry Mts. Bull. Int. Assoc. Eng. Geol. Bull. 16, 104–106.

Makos, M., Nitychoruk, J., Zreda, M., 2012. The Younger Dryas climatic conditions in the Za Mnichem Valley (Polisch High Tatra Mountains) based on exposure-age dating and glacier-climate modelling. Boreas 42, 745–761.

Makos, M., Nitychoruk, J., Zreda, M., 2013. Deglaciation chronology and paleoclimate of the Pięciu Stawów Polskich/Roztoki Valley, high Tatra Mountains, Western Carpathians, since the Last Glacial Maximum, inferred from ^{36}Cl exposure dating and glacier–climate modelling. Quat. Int. 293, 63–78.

Makos, M., Dzierżek, J., Nitychoruk, J., Zreda, M., 2014. Timing of glacier advances and climate in the High Tatra Mountains (Western Carpathians) during the Last Glacial Maximum. Quat. Res. 82, 1–13.

Mangerud, J., Andersen, S.T., Berglund, B.E., Donner, J.J., 1974. Quaternary stratigraphy of Norden, a proposal for terminology and classification. Boreas 4, 109–128.

McColl, S.T., 2012. Paraglacial rock-slope stability. Geomorphology 153–154, 1–16.

Mercier, D., Cossart, E., Decaulne, A., Feuillet, T., Jónsson, H.P., Sæmundsson, Þ., 2013. The Höfðahólar rock avalanche (sturzstrom): chronological constraint of para-glacial landsliding on an Icelandic hillslope. The Holocene 23, 432–446.

Montgomery, D.R., 2001. Slope distributions, threshold hillslopes, and steady-state topography. Am. J. Sci. 301, 432–454.

Moreiras, S.M., Hermanns, R.L., Fauqué, L., 2015. Cosmogenic dating of rock avalanches constraining Quaternary stratigraphy and regional neotectonics in the Argentine Central Andes (32° S). Quat. Sci. Rev. 112, 45–58.

Nagelisen, J., Moore, J.R., Vockenhuber, C., Ivy-Ochs, S., 2015. Post-glacial rock avalanches in the Obersee Valley, Glarner Alps, Switzerland. Geomorphology 238, 94–111.

Němčok, A., 1982. Zosuvy v slovenských Karpatoch. VEDA, Bratislava.

Němčok, A., Mahr, T., 1974. Kamenné ľadovce v Tatrách. Geogr. Cas. 26, 359–374.

Němčok, J., Bezák, V., Biely, A., Gorek, A., Gross, P., Halouzka, R., Janák, M., Kotański, Z., Lefeld, J., Mello, J., Reichwalder, P., Raczkowski, W., Roniewicz, P., Ryka, W., Wieczorek, J., Zelman, J., 1994. Geological Map of the Tatra Mountains. Ministerstvo Životného Prostredia Slovenské republiky, Bratislava.

Nishiizumi, K., Imamura, M., Caffee, M., Southon, J., Finkel, R., McAnich, J., 2007. Absolute calibration of ^{10}Be AMS standards. Nucl. Instrum. Methods Phys. Res., Sect. B 258, 403–413.

North Greenland Ice Core Project members, 2004. North Greenland Ice Core Project Oxygen Isotope Data. IGBP PAGES/World Data Center for Paleoclimatology Data Contribution Series 2004–059. NOAA/NGDC Paleoclimatology Program, Boulder CO, USA.

Orwin, J.F., Clague, J.J., Gerath, R.F., 2004. The Cheam rock avalanche, Fraser Valley, British Columbia. Landslides 4, 289–298.

Pagaczewski, J., 1972. Catalogue of earthquakes in Poland 1000–1970 years. Publications of the Institute of Geophysics. Acad. Sci. 51.

Pánek, T., 2015. Recent progress in landslide dating: a global overview. Prog. Phys. Geogr. 39, 168–198.
Penna, I.M., Hermanns, R.L., Niedermann, S., Folguera, A., 2011. Multiple slope failures associated with neotectonic activity in the Southern Central Andes (37°–37°30′S), Patagonia. Geol. Soc. Am. Bull. 123, 1880–1895.
Prager, C., Zangerl, C., Patzelt, G., Brandner, R., 2008. Age distribution of fossil landslides in the Tyrol (Austria) and its surrounding areas. Nat. Hazards Earth Syst. Sci. 8, 377–407.
Rasmussen, S.O., Biglerb, M., Blockleyc, S.P., Bluniera, T., Buchardta, S.L., Clausena, H.B., Cvijanovica, I., Dahl-Jensena, D., Johnsena, S.J., Fischerb, H., Gkinisa, V., Guillevica, M., Hoekf, W.Z., Lowec, J.J., Pedroa, J.B., Poppa, T., Seierstada, I.K., Steffensena, J.P., Svenssona, A.M., Vallelongaa, P., Vinthera, B.M., Walkerh, M.J.C., Wheatleyj, J.J., Winstrupa, M., 2014. A stratigraphic framework for abrupt climatic changes during the Last Glacial period based on three synchronized Greenland ice-core records: refining and extending the INTIMATE event stratigraphy. Quat. Sci. Rev. 106, 14–28.
Recorbet, F., Rochette, P., Braucher, R., Bourles, D., Benedetti, L., Hantz, D., Finkel, R.C., 2010. Evidence for active retreat of a coastal cliff between 3.5 and 12 ka in Cassis (South East France). Geomorphology 115, 1–10.
Rocscience, 2014. Rocscience DIPS from http://www.rocscience.com/products/1/Dips.
Schleier, M., Hermanns, R.L., Rohn, J., Gosse, J., 2015. Diagnostic characteristics and paleodynamics of supraglacial rock avalanches, Innerdalen, western Norway. Geomorphology 245, 23–39.
Selby, J.M., 1993. Hillslope Materials and Processes. Oxford University Press, Oxford.
Shroder, J.F., Owen, L.A., Seong, Y.B., Bishop, M.P., Bush, A., Caffee, M.C., Copland, L., Finkel, R.C., Kamp, U., 2011. The role of mass movements on landscape evolution in the central Karakoram: discussion and speculation. Quat. Int. 236, 34–47.
Soldati, M., Corsini, A., Pasuto, A., 2004. Landslides and climate change in the Italian Dolomites. Catena 55, 141–161.
Starkel, L., Soja, R., Michczyńska, D.J., 2006. Past hydrological events reflected in Holocene history of Polish rivers. Catena 66, 24–33.
Stead, D., Eberhardt, E., Coggan, J.S., 2006. Developments in the characterization of complex rock slope deformation and failure using numerical modelling techniques. Eng. Geol. 83, 217–235.
Stock, G.M., Uhrhammer, R.A., 2010. Catastrophic rock avalanche 3600 years BP from El Capitan, Yosemite Valley. Earth Surf. Process. Landf. 35, 941–951.
Stone, J.O., 2000. Air pressure and cosmogenic isotope production. J. Geophys. Res. 105 (B10), 23753–23759.
Sturzenegger, M., Stead, D., Gosse, J., Ward, B., Froese, C., 2015. Reconstruction of the history of the Palliser rockslide based on ^{36}Cl terrestrial cosmogenic nuclide dating and debris volume estimations. Landslides http://dx.doi.org/10.1007/s10346-014-0527-4.
Sweeney, C.G., Brideau, M.A., Augustinus, P.C., Fink, D., 2013. Lochnagar landslide-dam – Central Otago, New Zealand: geomechanics and timing of the event. In: Chyn, C.Y. (Ed.), Proceedings 19th NZGS Geotechnical Symposium, Queenstown. 20–23, pp. 1–8.
van Husen, D., Ivy-Ochs, S., Alfimov, V., 2007. Mechanism and age of late glacial landslides in the Calcareous Alps; The Almtal, Upper Austria. J. Earth Sci. 100, 114–126.
Wyllie, D.C., Mah, C., 2004. Rock Slope Engineering. Spon Press, Taylor & Francis Group, London and New York.
Yuan, Z., Chen, J., Owen, L.A., Hedrick, K.A., Cafee, M.W., Li, W., Schoenbohm, L.M., Robinson, A.C., 2013. Nature and timing of large landslides within an active orogen, eastern Pamir, China. Geomorphology 182, 49–65.
Zasadni, J., Kłapyta, P., 2014. The Tatra Mountains during the Last Glacial Maximum. J. Maps 10, 440–456.
Zerathe, S., Braucher, R., Lebourg, T., Bourlès, D., Manetti, M., Leanni, L., 2013. Dating chert (diagenetic silica) using in-situ produced ^{10}Be: possible complications revealed through the comparison with ^{36}Cl applied on coexisting limestone. Quat. Geochronol. 17, 81–93.
Zerathe, S., Lebourg, T., Braucher, R., Bourlés, D., 2014. Mid-Holocene cluster of large-scale landslides revealed in the Southwestern Alps by ^{36}Cl dating. Insight on an Alpine-scale landslide activity. Quat. Sci. Rev. 90, 106–127.
Zondervan, A., Hauser, T.M., Kaiser, J., Kitchen, R.L., Turnbull, J.C., West, J.G., 2015. XCAMS: the compact ^{14}C accelerator mass spectrometer extended for ^{10}Be and ^{26}Al at GNS Science. Nucl. Inst. Methods Phys. Res. B 361, 25–33 (in press).